Eine neue Methode der Zeiteichung der HADES-Driftkammern

Diplomarbeit

Khaled Teilab

Institut für Kernphysik
Johann Wolfgang Goethe-Universität
Frankfurt am Main

durchgeführt bei der
Gesellschaft für Schwerionenforschung Darmstadt

März 2007

Zusammenfassung

Das HADES-Experiment (**H**igh **A**cceptance **D**i**E**lectron **S**pectrometer) am SIS der GSI wurde zur Messung der e^+e^--Paare dileptonischer Zerfälle der leichten Vektormesonen im Energiebereich von $1 - 2\ AGeV$ entwickelt.

Eine der Hauptanforderungen an das Spurverfolgungssystem des Spektrometers ist eine Ortsauflösung von $100\ \mu m$, die benötigt wird, um die geforderte Massenauflösung von $1\ \%$ im Bereich der ω-Masse zu erzielen. Das Spurverfolgungssystem besteht aus vier Ebenen mit Vieldrahtdriftkammern (***M**ulti-wire **D**rift **C**hambers* (MDCs)) niedriger Massenbelegung (*low-mass*), die aus je 6 Auslesedrahtebenen bestehen.

Die primäre Messgröße von Driftkammern ist die Driftzeit der entlang einer Teilchenspur generierten Elektronen der Primärionisation zum Auslesedraht. Um die gemessene Driftzeit in eine Ortskoordinate umrechnen zu können, ist eine genaue Kenntnis der Ort-Zeit-Korrelation der Driftzellen und eine präzise Kalibrierung der gemessenen Zeiten nötig.

Im Rahmen dieser Arbeit wurde eine neue Methode zur Bestimmung der Kalibrierungsparameter der Driftzeiten mittels der Einkoppelung eines externen elektrischen Pulses auf die Drahtebenen der Driftkammern entwickelt und mit der herkömmlichen Methode der Kalibrierung verglichen.

Zur Kalibrierung wurden elektrische Pulse durch die Hochspannungsverteilung der Driftkammern auf die Potentialdrahtebenen geleitet und somit Signale auf die Signaldrähte induziert. Die Ausbreitungsgeschwindigkeit der Signale auf den Drähten, die zur Berücksichtigung der Laufzeiten benötigt wird, wurde experimentell bestimmt. Die Genauigkeit der Methode zur Bestimmung der Kalibrierungsparameter übertrifft die Auflösung der Driftzeitmessung der Driftkammern. Die Kalibrierung der Driftzeiten benötigt nur wenig Rechen- und Zeitaufwand und stellt die Kalibrierungsparameter in gleich hoher Präzision für alle Driftzellen zur Verfügung. Die Qualität der Kalibrierung wird im Gegensatz zur herkömmlichen Methode prinzipbedingt nicht durch Fluktuationen der Startzeit des jeweiligen Stoßereignisses und die Flugzeit der dabei emittierten Teilchen zu den Driftzellen, sowie des elektronischen Rauschens beeinflusst. Die Qualität der Kalibrierung konnte gegenüber der herkömmlichen Methode signifikant verbessert werden.

Die Auswirkung der Kalibrierungsparameter auf die Spurrekonstruktion wurde untersucht und für die beiden Kalibrierungsmethoden verglichen. Die Ergebnisse lassen keinen eindeutigen Schluss auf die Auswirkung der Fehler in der Kalibrierung auf die Qualität der Spurrekonstruktion zu, da die Ergebnisse der Spurrekonstruktion von anderen Effekten dominiert werden.

Contents

List of Figures

List of Tables

Chapter 1

Introduction

The study of nuclear matter at high temperature and density is one of the main fields of physics research nowadays. The aim of these studies is a better understanding of the equation of state of the nuclear matter, and to examine the expectations of the fundamental theory of strong interactions, the quantum chromo dynamics (QCD). Compressed nuclear matter plays an important role in astrophysical processes, for example; the stability of neutron stars, or the supernova explosions. Through the invention of particle accelerators, it has been possible to systematically study the nuclear matter at high temperature and density in the laboratory.

Under normal conditions, the nuclear matter is a many body system composed of protons and neutrons, which are bound together via the strong interaction. The constituents of the nucleons, *i.e.* the quarks, which cannot be observed as free particles, interact with each other by the exchange of gluons.

The coupling constant of the strong interaction is energy dependent. At high energies, the coupling constant becomes small and the perturbation theory can be applied to describe the processes. For low energies, however, the coupling is strong, and the perturbation theory cannot be applied. For the latter, different models have been developed, which take into account the mesonic and baryonic degrees of freedom of the system considered. These models expect a change in the properties of hadrons in nuclear matter, caused by a restoration of chiral symmetry and by coupling between mesons and baryons. The interaction of vector mesons with the surrounding matter was described by different hadronic models, based on effective and mean field theories. The spectral functions of vector mesons change in nuclear matter. Calculations for the ρ-meson predict a reduction of the effective mass, already at normal nuclear density.

In a heavy ion collision, the vector mesons, and especially the ρ-meson, work

as a probe for the observation of the chiral symmetry restoration. The ρ-meson decays during the hot dense phase of the heavy ion collision, since it has a short life time of 1.3 fm/c. Vector mesons decay into dileptonic channels with a typical branching ratio of around 10^{-4}, and their decay products are ideal probes for the study of their properties, since they leave the nuclear matter without undergoing strong interaction. The e^+e^- pairs carry therefore information about the properties of the vector meson at the moment of decay like the mass and decay width in the medium.

The HADES- (**H**igh **A**cceptance **D**i**E**lectron **S**pectrometer) experiment at the SIS at GSI was developed to measure the e^+e^- pairs of the dileptonic decay of vector mesons in the energy range of 1-2 $AGeV$. With its high acceptance, high resolution, and high rate processing capability, the HADES spectrometer offers a possibility to systematically study the properties of vector mesons in nuclear matter. It was designed to have a mass resolution of 1% in the mass region of the ω-meson ($\sim 0.8\ GeV/c^2$).

Motivation

To achieve the aimed mass resolution of the HADES spectrometer, a position resolution of 100 μm in the tracking system of HADES is required. In the framework of this thesis, a new method for the determination of the calibration parameters of the drift chambers (the main part of the tracking system, see chapters 2 and 3) using an external electrical pulse has been investigated. The up to now used calibration method which is based on the measured times during an experiment has the following shortcomings:

- The data based method needs a large amount of statistics and is therefore time consuming.
- The quality of the obtained calibration parameters is highly affected by noise.
- Some systematic effects, arising from the time-of-flight of the particles to the chambers, the fluctuations in the experiment trigger, and the low statistics at high polar angles far from the beam axis, impact on the quality of the track reconstruction.

The new method needs much lower statistics, is less affected by noise, and offers the same statistics for all readout channels, thus promises an improvement of the position resolution of the track reconstruction.

Chapter 2

The HADES spectrometer

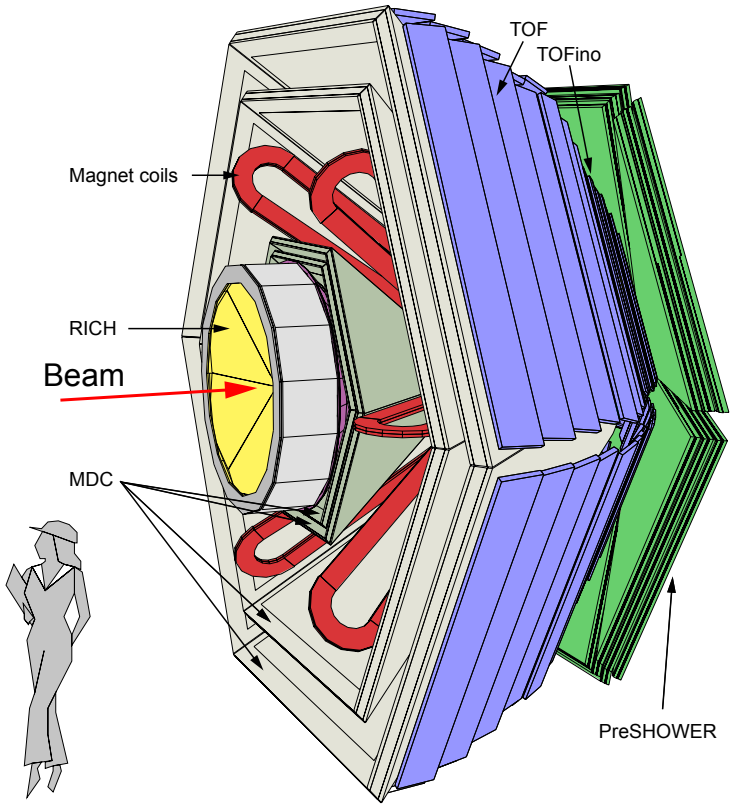

Figure 2.1: 3-dimensional view of the HADES spectrometer.

The HADES spectrometer consists of the following sets of systems:

- START and VETO detectors

- **R**ing **I**maging **Ch**erenkov detector (RICH)
- Magnet
- **M**ulti-wire **D**rift **C**hambers (MDC)
- **T**ime **O**f **F**light detectors (TOF and TOFino)
- Pre-Shower detector

2.1 START and VETO detectors

The START and VETO detectors, are two identical diamond detectors placed 75 cm in front of and behind the target respectively. They operate in an anti-coincidence logic, such that when a beam particle detected by the START detector, passes through the target without interaction, the particle is detected by the VETO detector as well, and the corresponding event is discarded. The detectors have a size of $25 \times 15\ mm$, and a thickness of $100\ \mu m$ to reduce the effect of multiple scattering and the production of secondary beams. The START detector provides the time of a reaction in the target with a precision of 50 ps.

2.2 Ring Imaging Cherenkov detector (RICH)

When a charged particle passes through a medium of refractive index n with a velocity $\beta > 1/n$, it emits Cherenkov radiation. The radiation is emitted when a charged particle moves through a medium with a velocity greater than the phase velocity of light in the medium. The particle polarizes the surrounding medium creating dipoles. At these high velocities, the polarization is not symmetric, but mainly focused in the direction of particle movement. A coherent radiation is emitted on a defined light cone (Cherenkov radiation).

The threshold for the emission of Cherenkov radiation in the C_4F_{10} radiator gas used in the RICH detector is $\gamma_{thresh} = 18.3$. Hadrons emitted in reactions at the SIS energies of 2 $AGeV$, have a maximum γ value of 10. Therefore they are not detected by the RICH. e^-e^+ with energies above 10 MeV produce Cherenkov radiation in the RICH. Hence, the RICH detector can be used for a *real-time* lepton identification in HADES.

Electrons moving through the RICH produce Cherenkov light in a cone along their trajectories. The light is reflected by the aluminized carbon fiber mirror,

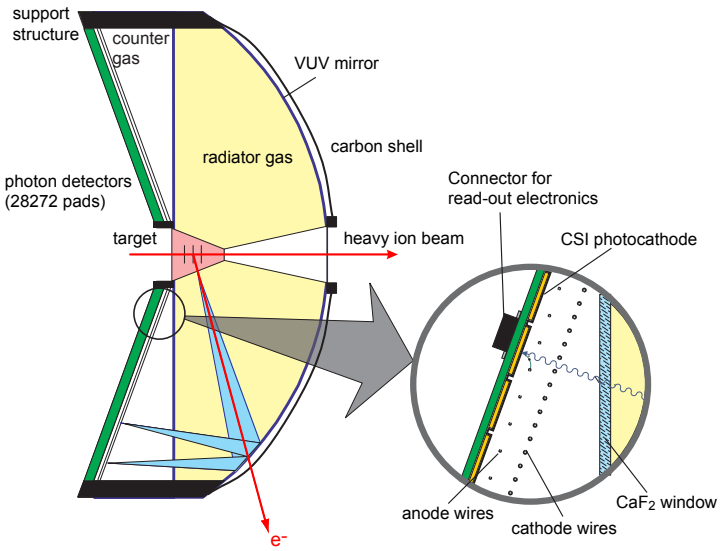

Figure 2.2: Schematic representation of the RICH detector.[Böh99].

and is focused as an elliptical image on the position sensitive photon detector. The photon detector is separated by a 5 mm thick CaF_2 window from the radiator volume. It is composed of three multi wire proportional chambers with a segmented photocathode. The Cherenkov light releases photoelectrons from the photo cathode, inducing an electric signal on the photocathode in one or more pads.

2.3 Magnet spectrometer

The magnet of the HADES experiment is composed of 6 super conducting toroidal coils arranged around the beam axis. The maximum electrical current of the magnet is 3665 A, at a temperature of 4.6 K. The magnetic field strength reaches, 3.7 T inside the coils, 2.4 T near the coils, and $\sim$ 0.8 T in the middle between two coils. The magnet of the HADES experiment has to fulfill the following requirements:

- High geometrical acceptance. The magnet coils have to be compact to minimize the dead regions of the detector.
- The magnetic field strength in the region of RICH and MDC's has to be kept as low as possible.

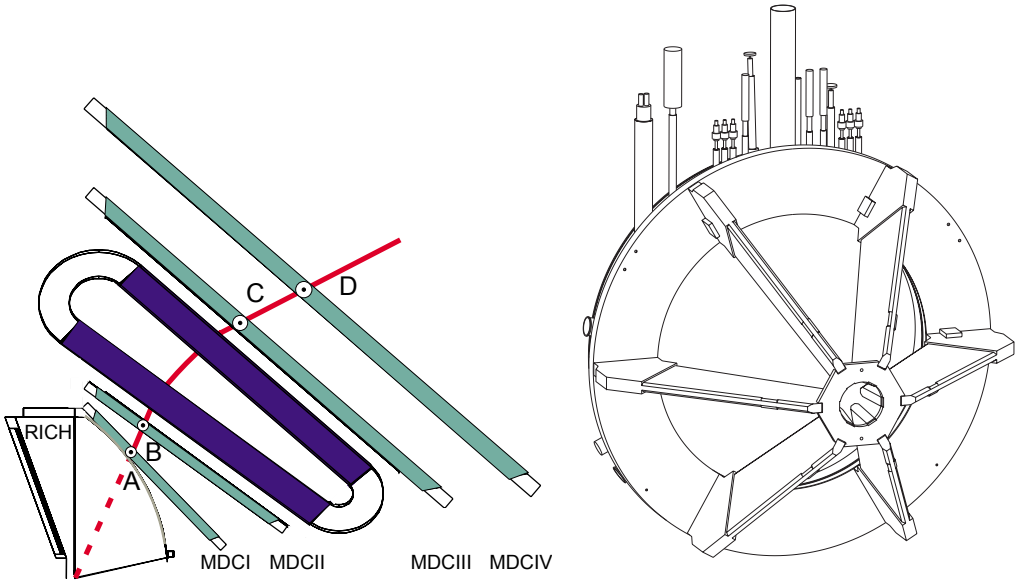

(a) (b)

Figure 2.3: (a) Working principle of the magnet spectrometer [Lip00]. The momentum of a charged particle can be determined from the bending angle of the particle trajectory inside the magnetic field, if the field strength is known. (b) View of the magnet of the HADES spectrometer.

- Acceptance of particles with a large momentum range, within a large solid angle.

Together with the MDC's, the magnet of the HADES experiment constitutes the tracking system of HADES. The construction of the MDC's will be described in details in chapter 3.

2.4 Multiplicity Electron Trigger Array (META)

The META consists of the two time-of-flight systems TOF and TOFino covering the whole HADES acceptance, as well as the Pre-Shower system at polar angles $\theta < 45°$. It is used for particle identification and event selection purposes based on the multiplicity of particles.

2.4.1 TOF and TOFino

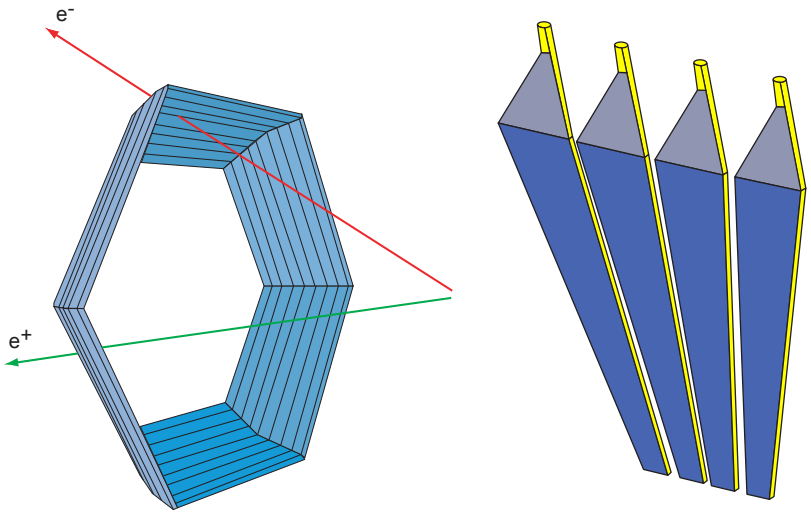

(a) (b)

Figure 2.4: Schematic view of (a) the TOF detector and (b) one sector of the TOFino detector.

The TOF detector is used to measure the time-of-flight of particles from the target to the TOF itself. It is arranged in 6 sectors, each is composed of 8 modules. Each module in the TOF detector consists of 8 plastic scintillation rods, and a **P**hoto **M**ultiplier **T**ube (PMT) at each end of the rod. When hit by a particle, the scintillation rod provides a light signal which is collected at both ends by the PMT's, and is converted to a time signal using a TDC (**T**ime to **D**igital **C**onverter). Using the time information from both ends, one can calculate the time-of-flight of the particle and the position of the hit in the rod.

The TOF detector covers the polar angular range $44^\circ < \theta < 88^\circ$. For $\theta < 45^\circ$ the TOFino detector is used to provide the time-of-flight information. The TOFino detector is similar to the TOF, nevertheless with a lower granularity. It is divided into 6 sectors, each sector composed of 4 scintillator paddles arranged radially around the beam axis (see figure 2.4). The scintillator light in the TOFino detector is collected only at one end of the paddle. Therefore, the position information of the particle hit cannot be obtained using the TOFino system alone. Only after the correlation with the information from the PreSHOWER detector, the particle hit position can be determined.

2.4.2 PreSHOWER

The PreSHOWER detector is mounted behind the TOFino detector and covers the range of polar angle $18° < \theta < 45°$. It is divided into 6 sectors, each of them consisting of three nearly identical multi wire chambers *(pre-converter, post 1, post 2)* (figure 2.5). Two lead converters of 1.12 cm and 0.84 cm thickness are placed between the three wire chamber. Each wire chamber is composed of one cathode layer, one wire layer, and another segmented cathode layer. The wire layer consists of alternating anode and cathode wires. The chambers are filled with an $Argon/i - butane/heptane$ gas mixture and are operated at a cathode potential of -3200 V.

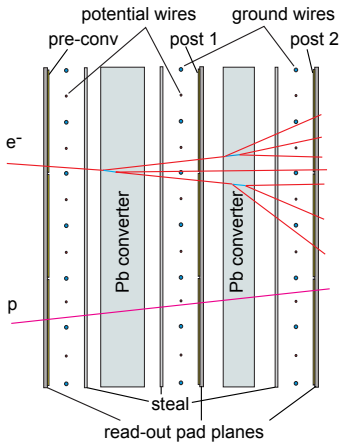

Figure 2.5: Schematic representation of the PreSHOWER detector.

Relativistic charged particles passing through the lead converter emit photons through *bremsstrahlung*. The emitted photons can convert to e^+e^- pairs by the process of pair production. If the conversion products have enough energy, they can undergo the same process as the primary particle. At the end a *shower* of electrons and positrons is created (see figure 2.5). The charged particles passing through the wire chambers ionize the molecules of the counting gas. The electrons produced by ionization move towards the anodes of the chamber where they get multiplied by an avalanche process. The avalanche results in a positive signal on the neighboring pads of the segmented cathode layer which is readout by the electronics. Through a comparison between the detected charges in the different chambers, one can deduce if a shower has been produced. In the range of energies provided by the SIS only leptons produced in a heavy ion collision will have enough energy to produce a shower. The heavy hadrons instead, have a very small probability of emitting bremsstrahlung and hence producing a shower.

Chapter 3

The HADES multi-wire drift chambers

The tracking system of the HADES-spectrometer consists of four planes of multi-wire drift chambers. Each plane is divided into six identical trapezoidal drift chambers (MDC's). Each MDC covers one sector of the spectrometer. Hence, the total number of drift chambers in the spectrometer is 24.

3.1 Construction

In the construction of the drift chambers the following requirements had to be taken into account:

- The chambers frames are subjected to high tension forces through the wires connected to them. Since the tracking system has to provide low material budget and a high geometrical acceptance, the space available for the the frames is very limited. These conditions imply a sophisticated design and selection of the materials to ensure the mechanical stability of the chambers.
- The materials were chosen such that, the required drift cell intrinsic resolution of less than $140\ \mu m$ is not lost by the thermal expansion.
- The glues and other chemical materials used in the construction of the chambers have been chosen such that, they do not provide a source of impurity in the chambers. These components can emit solvent containing substances, which negatively affect the efficiency of the gas, and accelerate the aging process in the chamber.

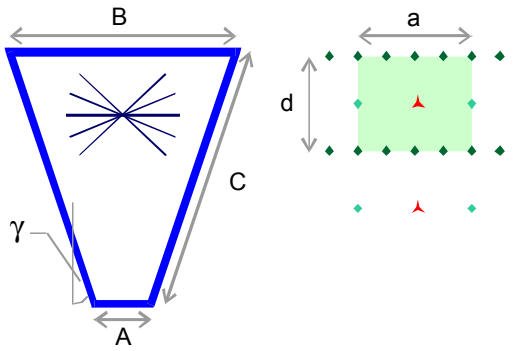

Figure 3.1: Dimensions of the drift chamber [Str98].

Plane no.	A $[mm]$	B $[mm]$	C $[mm]$	γ $[°]$	a $[mm]$	d $[mm]$	Area $[m^2]$	Volume $[l]$
I	139,21	767,38	839,19	21,98	5	5	0,34	11,99
II	205,00	905,00	1049,27	19,49	6	5	0,49	20,58
III	310,43	1804,80	2139,05	20,44	12	8	1,88	150,4
IV	345,46	2224,05	2689,04	20,44	14	10	2,83	197,8
per sector							5,54	380,77
Total							33,24	2284,62

Table 3.1: Dimensions of the drift chamber [Str98]

The dimensions of the trapezoidal chambers of the four planes range from ca. $77 \times 84\ cm^2$ (figure 3.1), for the most inner plane, up to $222 \times 269\ cm^2$ for the most outer plane. Table 3.1 shows the dimensions and sizes of the different chambers, and the cell dimensions for each of them.

Each drift chamber is composed of 6 field/signal wire layers, which are surrounded by two cathode wire layers. A drift cell is built from one signal wire, the two neighboring field wires, and the cathode wires of the two surrounding cathode layers.

As shown in figure 3.2, the wires of each layer are oriented at a different angle relative to the coordinate system of the chamber. The angles of the field/signal layers vary between $+40\,°$, $-20\,°$, $+0\,°$, $-0\,°$, $+20\,°$ and $-40\,°$, where the sign defines the direction of the rotation of the wires (see table 3.2). The two $\pm 0\,°$-layers are shifted, relative to each other, by an amount equal to one half of the width of a drift cell. The wires of all cathode layers are oriented at an angle of $90\,°$ relative to the chamber coordinate system.

Using special winding machines, with a precision of $20\ \mu m$, the wires have been put in their position on a Stesalite frame [Bou94], and glued using Hexcel

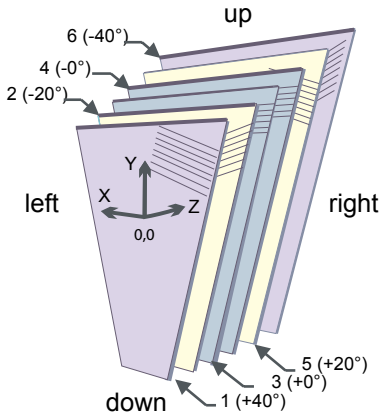

Figure 3.2: Orientation of the wire layers of the drift chambers.

	Angle [°]
Layer 1	+ 40
Layer 2	- 20
Layer 3	+ 0
Layer 4	- 0
Layer 5	+ 20
Layer 6	- 40
Cathode layers	90

Table 3.2: Angle of the wires of the wire layers.

Epoxide glue [Bou96] [Gar98]. Both materials fulfill the requirement concerning the minimization of the contamination of the counting gas with chemical solvents, which eventually can result in aging effects under the influence of ionizing radiation.

The distances between the cathode and signal layers, and between the signal and field wires, define the dimensions of the drift cells for the different chamber planes. These dimensions range from $5 \times 5\, mm^2$, for the most inner plane (MDC-I), up to $14 \times 10\, mm^2$, for the most outer plane (MDC-IV) (see figure 3.1 and table 3.1).

	Material	Diameter $[\mu m]$	
Cathode wires	Aluminium (Al)	80_{I-III}	100_{IV}
Field wires	Aluminium (Al)	80_{I-II}	100_{III-IV}
Signal wires	Gold plated Tungsten (Au/W)	20_{I-III}	30_{IV}

Table 3.3: Properties of the wires used in the drift chambers. Indices indicate the different planes.

Table 3.3 shows the properties of the different wires used in the chambers. In addition, the entrance and exit windows of the chambers are built using $12\ \mu m$ Mylar foils coated with Aluminium [Gar98]. The materials were chosen to minimize the effect of multiple scattering of the particles on the momentum resolution of the tracking system.

3.2 Data acquisition

One of the important constraints for the development of the readout electronics for the HADES drift chambers is the large number of readout channels. The total number of channels which have to be readout in each triggered event is about 27000. The readout electronics of the drift chambers are mounted on the drift chambers frames. It is impossible, for the design of HADES, to transport the analog readout signals of the chambers through cables to external readout electronics. Consequently, the readout electronics had to fulfill the following constraints:

- The drift chamber data are digitalized on the chambers themselves.
- The electronics must not reduce the acceptance of the detector. They should be placed in the non-active volume of the detector.
- The readout electronics should not be placed in the region of high beam intensity, which can damage them. Also the electronics must be stable under the effect of ionizing radiation (*radiation hard*).

The arguments mentioned require having a compact readout electronic system. The system must offer a high density of readout channels and a low power consumption to operate in areas of the detector, where the available space is limited without requiring a sophisticated active cooling system.

The readout electronics are placed on the three long sides of each drift chamber (figure 3.3(a)). One channel of an 8-channel **A**mplifier **S**haper **D**iscriminator chip (ASD8) [New93] and one channel of an 8-channel **T**ime to **D**igital **C**onverter (TDC) chip [TDC98] are assigned to each signal wire. The ASD8 amplifies, shapes, and discriminates the analog signal of the drift charges. The TDC determines the start time and the width of the logical signal provided by the ASD8 relative to an external *common-stop* signal (CMS).

There are two types of motherboards; short motherboards containing 8 TDC chips with a total number of 64 channel, and long motherboards containing 12 TDC chips with a total number of 96 channels. 4 or 6 daughterboards are mounted on each motherboard depending on its length. Each daughterboard contains two ASD8 chips. Each MDC-I drift chamber has 14 motherboards, while other chambers have 16 motherboards.

Every two or three motherboards are read out in a chain by the same **R**ead-**O**ut **C**ontroller (ROC). The configuration of the chains is optimized such that the amount of data transferred through each chain of one chamber is almost the same. The data are read out and buffered by the ROC. In the concentrator module,

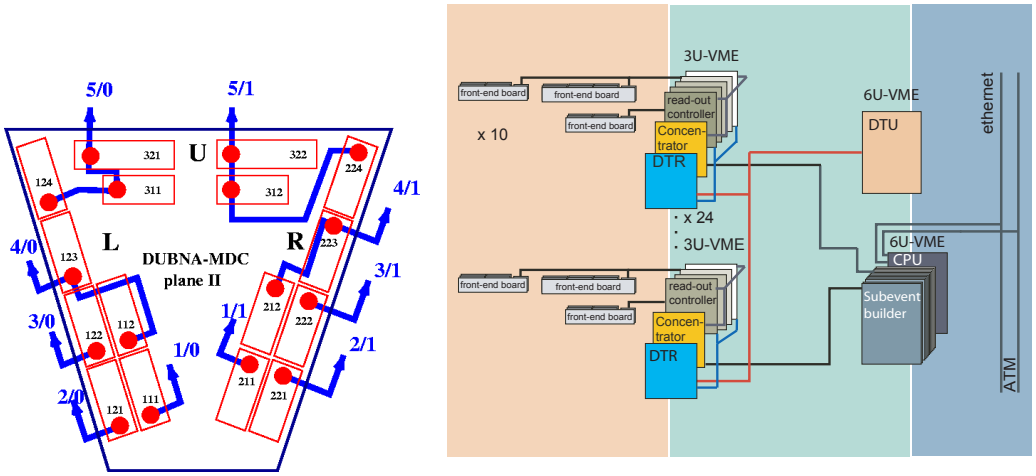

(a) (b)

Figure 3.3: (a) Schematic diagram of the positioning of the motherboards relative to the chamber for plane II. The blue lines mark the chains of motherboard readout by the same read-out-controller [Mdc04]. (b) Data acquisition scheme of the drift chambers.

the conversion of the ROC **LVDS** signals *(low voltage differential signal)* to the SAM (**S**teuerungs- und **A**uslese**m**odul) TTL signals *(transistor transistor logic)* takes place. The SAM builds the *sub-events* of the drift chamber from the data words of the individual TDC channels. The SAM data are sent to the central *event builder* of the data acquisition, which builds a common event from the different sub-events of the different detector systems. The events are saved on a hard disc or on a magnetic tape.

A so-called *common-stop* trigger (CMS) is generated by the START-detector and the time-of-flight wall (TOF/TOFino). This trigger is sent to the ROC from the central trigger unit (CTU) through the detector trigger unit (DTU) and the trigger receiver card (DTR). The common stop trigger is distributed from the ROC's to the TDC's where it stops the self triggered time measurement of the TDC. A schematic representation of the readout concept is depicted figure 3.3 (b). The measurement concept of the drift chambers, will be described in details in chapter 5.

Chapter 4

Drift chambers physics

The multi-wire drift chambers of the HADES spectrometer are used for the purpose of tracking of charged particles resulting from the nuclear collisions between beam and target nuclei. They belong to a wide family of detectors used in the field of high energy and nuclear physics. The detection of charged particles in this group of detectors is based on the measurement of electron-ion pairs produced by the passage of the particle through a gaseous medium. In this chapter, the physics of operation of gas detectors will be briefly described.

4.1 Interaction of charged particles in gases

When a fast charged particle traverses a gaseous medium, it looses some part of its energy through the interaction with the atoms and molecules of the medium. The most probable type of interaction, and the one relevant for gas detectors, is the Coulomb interaction between the electromagnetic fields of the incoming charged particle and the medium atoms, resulting in the excitation and ionization of the atoms and molecules of the gas itself.

4.1.1 Energy loss due to electromagnetic interactions

In the framework of relativistic quantum mechanics, an expression for the average differential energy loss by ionization and atomic excitation has been obtained in 1930 by Bethe and Bloch and is known as the Bethe-Bloch equation (equation 4.1.1).

$$-\frac{dE}{dx} = 4\pi N_A r_e^2 m_e c^2 z^2 \frac{Z}{A}\frac{1}{\beta^2}\left[\frac{1}{2}\ln\left(\frac{2m_e c^2\beta^2\gamma^2 T_{max}}{I^2}\right) - \beta^2 - \frac{\delta(\beta\gamma)}{2}\right] \quad (4.1)$$

with

N_A	- Avogadro's number
r_e	- Classical electron radius
m_e	- Electron mass
z	- Charge of incident particle
Z	- Atomic number of absorber
A	- Atomic mass of absorber
I	- Mean excitation energy
$\delta(\beta\gamma)$	- Density effect correction to ionization energy loss

and T_{max} is the maximum kinetic energy which can be imparted to a free electron in a single collision:

$$T_{max} = \frac{2m_e c^2 \beta^2 \gamma^2}{1 + 2\gamma m_e/M + (m_e/M)^2} \tag{4.2}$$

M - Mass of the incident particle

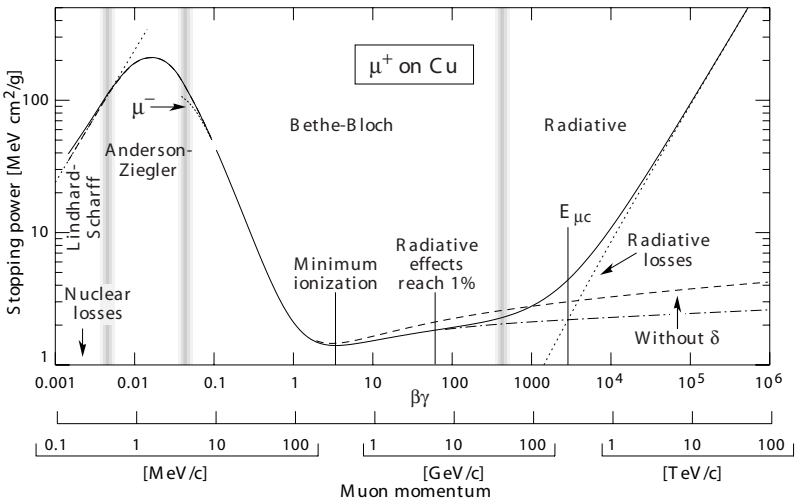

Figure 4.1: Stopping power $(= \langle -dE/\rho dx \rangle)$ for positive muons in copper as a function of $\beta\gamma = p/Mc$ over nine orders of magnitude in momentum. Solid curves indicate the total stopping power. [PDG06]

As an example, figure 4.1 shows the rate of energy loss of muons in copper as a function of the muon momentum. Considering the part of the figure described by

equation 4.1.1, the amount of energy loss through ionization and atomic excitation decreases rapidly dominated by the $1/\beta^2$ term. It reaches a minimum at $\beta \simeq 0.97$, and eventually increases logarithmically with $\beta\gamma$ (relativistic rise). In practical cases, most relativistic particles (*e.g.* cosmic-ray muons) have mean energy loss rates close to the minimum, and are called "minimum ionizing particles". As the particle energy increases, its electric field flattens and extends, so that it can ionize atoms at far distances from its trajectory. However, real media become polarized, limiting the field extension and effectively reducing this relativistic rise. Hence, the density effect term gives the correction of the energy loss in this region, otherwise it would be overestimated by the logarithmic rise with $\beta\gamma$. Figure 4.1 shows the rate of energy loss with and without the density effect correction.

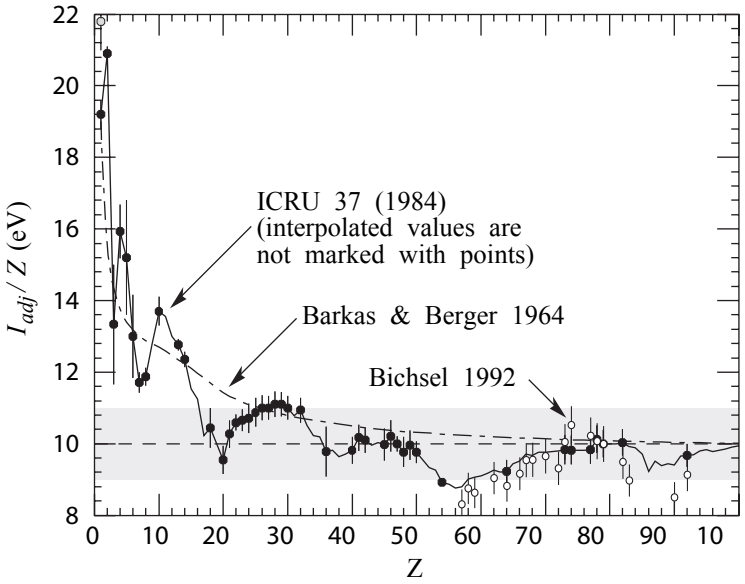

Figure 4.2: Mean excitation energies (divided by Z) as adopted by the ICRU [ICR84]. Those based on experimental measurements are shown by symbols with error flags; the interpolated values are simply joined. The grey point is for liquid H_2; the black point at 19.2 eV is for H_2 gas.

A minor dependence on the mass of the incident particle at the highest energies is introduced through T_{max}, but for all practical purposes in high-energy physics dE/dx in a given material is a function only of β. In most materials , particles of the same velocity have similar rates of energy loss; there is a slow decrease in the rate of energy loss with increasing Z as A tends to be greater than Z.

The electromagnetic energy loss in a material is the result of a small number of discrete interactions. The individual events can be classified into two groups:

- close collisions, with large energy transfers resulting in the release of electrons (ionization).
- distant collisions, with smaller energy transfers resulting in both ionization and atomic excitation.

Primary ionization and excitation contribute almost equally to the amount of energy loss. The value of the mean excitation energy is in general the result of a measurement for each material. Figure 4.2 [PDG06] shows the mean excitation energy as a function of Z either measured or interpolated for materials with Z up to 100.

4.1.2 Energy loss distribution

Since the total energy loss in thin materials is given by a small number of discrete interactions with a wide range of possible energy transfers, the energy loss distribution is described by a Landau distribution:

$$\Phi(\lambda) = \frac{1}{2\pi i} \int_{c-i\infty}^{c+i\infty} \exp\left(s \ln s + \lambda s\right) ds. \tag{4.3}$$

approximated by:

$$M(\lambda) = \frac{1}{\sqrt{2\pi}} \exp\left(-\frac{1}{2}(\lambda + e^{-\lambda})\right). \tag{4.4}$$

where λ is the deviation of the energy loss from the most probable value $(\Delta E)_{mp}$, normalized to the value of the average energy loss $\langle \Delta E \rangle$ [Sau77].

$$\lambda = \frac{\Delta E - (\Delta E)_{mp}}{\langle \Delta E \rangle}. \tag{4.5}$$

Figure 4.3 shows the distribution of the energy loss in matter in a single collision. The units in the figure are arbitrary. The long tail of the Landau distribution at very high energy transfers corresponds to the events where one or more energetic electrons have been produced.

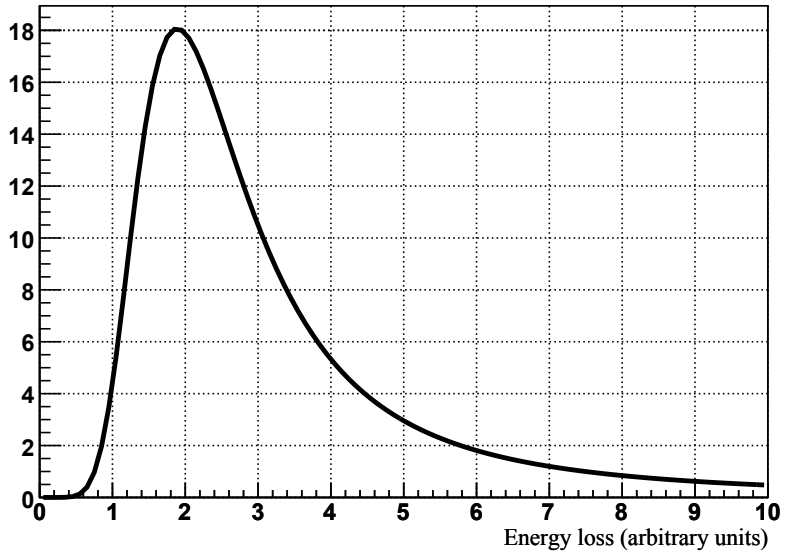

Figure 4.3: Distribution of the energy loss in matter in a single collision. The units on the axes are arbitrary. The energy loss follows a landau distribution and has a maximum at the value of the most probable energy loss.

4.1.3 Primary and total ionization

Electrons released by the particle passage through the gas *(primary electrons)* can have enough energy (greater than the ionization energy of the medium) to further ionize other atoms and release *secondary electrons*. The sum of the both contributions is called the total ionization, and the total number of electron-ion pairs per cm is given by:

$$n_T = \frac{\Delta E}{W_i} \qquad [1/cm], \tag{4.6}$$

where ΔE is the total energy loss in one cm of the medium and W_i is the effective average energy to produce one pair [Sau77]. Table 4.1 gives the values of n_T and W_i for some gases at atmospheric pressure together with the average energy loss for minimum ionizing particles.

For gas mixtures the following law applies:

$$n_T = \sum n_{Tj} c_j \tag{4.7}$$

where n_{Tj} is the total ionization for the same thickness of gas j and c_j is the concentration of j in the mixture.

Gas	W_i *(eV)*	$\langle dE/dx \rangle$ *(keV/cm)*	n_T *(pair/cm)*
H_2	37	0.34	9.2
He	41	0.32	7.8
Ar	26	2.44	94
C_4H_{10}	23	4.5	195

Table 4.1: Properties of some gases used in drift chambers. The values of energy loss and ion pairs per unit length are given at atmospheric pressure for minimum ionizing particles

The gas mixture used in the HADES drift chambers consists of 60% He and 40% iC_4H_{10}. Computing the number of total ion pairs produced in 1 cm of this mixture for minimum ionizing particles at normal conditions using values of table 4.1 gives:

$$n_T = 0.6 \times 7.8 + 0.4 \times 195 = 83\ (pairs/cm) \tag{4.8}$$

Hence, the number of ion pairs produced by a minimum ionizing particle passing vertically through one cell of a plane IV chamber is 83 (see table 3.1).

4.2 Drift and diffusion of charges in gases

4.2.1 Diffusion in absence of an external electric field

Charges produced by the passage of an ionizing particle through a gas loose their energy by multiple collisions with the gas molecules. Assuming thermal equilibrium, their energy distribution is given by the kinetic theory of gases with an average kinetic energy of:

$$\langle \epsilon \rangle = 3/2\ kT \tag{4.9}$$

and following the Maxwell-Boltzmann distribution:

$$F(\epsilon) = const\sqrt{\epsilon}\ e^{(-\epsilon/kT)}. \tag{4.10}$$

where k is the Boltzmann constant and T is absolute temperature. This localized distribution of charges diffuses by multiple collisions following a Gaussian law [Sau77]:

$$\frac{dN}{N} = \frac{1}{\sqrt{4\pi Dt}} e^{(-r^2/4Dt)} dr, \tag{4.11}$$

where D is the diffusion coefficient and dN/N is the fraction of charges found in an element dr at a distance r and time t from the origin. The diffusion coefficient

depends strongly on the applied electric field, this will be discussed in the next sections. The standard deviation of the distribution is given by:

$$(a) \quad \sigma_r = \sqrt{2Dt} \quad or \quad (b) \quad \sigma_v = \sqrt{6Dt} \tag{4.12}$$

for a linear and a volume diffusion respectively. Having a small mass and negligible size, the electrons move much faster than ions during diffusion, and their mean free path is about four times that of ions.

4.2.2 Drift of ions

When an electric field is applied across the gas volume, the ions created along the trajectory of the ionizing particle start to drift in the direction of the field. The average velocity W^+ of this drift motion is linearly proportional to the reduced field E/P, where P is the gas pressure. The quantity mobility is defined as:

$$\mu^+ = \frac{W^+}{E/P} \tag{4.13}$$

and the following relation holds between mobility and diffusion coefficients [Sau77]:

$$\frac{D^+}{\mu^+} = \frac{kT}{e} \tag{4.14}$$

Values of the mobility and diffusion coefficients are specific for each ion moving in a given gas. In gas mixtures, the mobility ${\mu_i}^+$ of the ion ${G_i}^+$ is given by Blanc's law:

$$\frac{1}{{\mu_i}^+} = \sum_j \frac{c_j}{{\mu_{ij}}^+} \tag{4.15}$$

where c_j is the concentration of gas j in the mixture and ${\mu_{ij}}^+$ the mobility of ion ${G_i}^+$ in gas G_j. However an effective process of charge transfer takes place in gas mixtures, and quickly removes all ions except the ones with the lowest ionization potential. Depending on the nature of the ion and on the difference in the ionization potential, it takes an ion between 100 and 1000 collisions to transfer its charge to a molecule having a lower ionization potential [Sau77]. After a very short time, the charge-exchange mechanism will leave only one kind of ions drifting. In the case of the $He/i-butane$ mixture used in the HADES drift chambers, only $i-butane$ carries the charge and drifts to the potential wires since its mean excitation energy is lower than that of He.
Ions migrating in a time t over a length ℓ in the direction of the applied field diffuse according to equation 4.11. The standard deviation is given by equation 4.16:

$$\sigma_\ell = \sqrt{2D^+t} = \sqrt{\frac{2kT\mu^+t}{e}} = \sqrt{\frac{2kTPW^+t}{eE}} = \sqrt{\frac{2kTP\ell}{eE}} \tag{4.16}$$

from which it is clear that σ_ℓ depends only on the applied electric field at constant temperature and pressure, and is independent of the nature of the ions and gas.

4.2.3 Drift of electrons

In the case of ions, and due to there heavy mass, the average energy of ions stays almost unmodified up to very high values of the applied electric field. This leads to a constant mobility for ion. For electrons this is not the case. Due to their small mass, electrons can substantially increase their energy between collisions under the influence of the electric field.
The drift velocity of electrons can be written as [Sau77]:

$$W = \frac{e}{2m_e} E\tau \tag{4.17}$$

where τ is the average time between collisions, and is a function of the electric field E. The collision cross section σ and consequently τ varies strongly with E, going through maxima and minima. This is called the Ramsauer effect, and arises from the fact that the electron wavelength approaches those of the electron shells of the gas molecules leading to complex quantum mechanical processes. The average energy of the electrons can therefore exceed the thermal value by many orders of magnitude, and the energy distribution changes from the original Maxwell-Boltzmann shape. Figure 4.4 [Mar05] shows the dependence of the electrons drift velocity on the reduced electric field for different mixtures of $He/i-butane$. The change in the drift velocity with increasing field is not constant over the range shown.

If both the elastic and inelastic collision cross sections are known, the following expression for the energy distribution of electrons can be deduced, assuming that the electric field is not so high, such that only a negligible fraction of the electrons undergo ionizing collisions [Sau77]:

$$F(\varepsilon) = const\sqrt{\varepsilon} \quad exp\left(-\int \frac{3\Lambda(\varepsilon)\varepsilon d\varepsilon}{[eE\lambda(\varepsilon)]^2 + 3\varepsilon kT\Lambda(\varepsilon)}\right) \tag{4.18}$$

where the mean free path, $\lambda(\varepsilon)$, is given by:

$$\lambda(\varepsilon) = \frac{1}{N\sigma(\varepsilon)} \tag{4.19}$$

with N as the total number of molecules per unit volume, and $\sigma(\varepsilon)$ is the collision cross section. $\Lambda(\varepsilon)$ is the fraction of energy lost on each impact *(inelasticity)*.

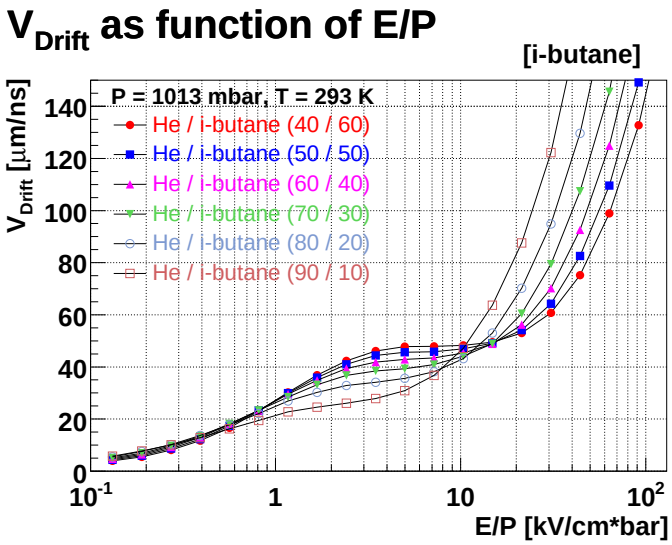

Figure 4.4: Variation of the drift velocity of electrons as a function of the reduced field for different $He/i-butane$ mixtures. The reduced field in the drift chambers of HADES in operation ranges around 1-10 kV as shown in figure 4.7 .(b) [Mar05].

If $F(\varepsilon)$ is computed, the drift velocity and the diffusion coefficients of electrons as a function of the electric field are given by:

$$W(E) = -\frac{2}{3}\frac{eE}{m}\int \varepsilon\lambda(\varepsilon)\frac{\partial[F(\varepsilon)u^{-1}]}{\partial\varepsilon}d\varepsilon \tag{4.20}$$

and

$$D(E) = \int \frac{1}{3}u\lambda(\varepsilon)F(\varepsilon)d\varepsilon \tag{4.21}$$

where $u = \sqrt{2\varepsilon/m}$ is the instant velocity of electrons with energy ε.

4.2.4 Electronegative gases

Electrons drifting in a gas mixture can get captured by electronegative molecules in the mixture. The attachment coefficient of noble gases is zero; they are unable to capture electrons. Polyatomic gases such as $i-butane$ have a finite attachment coefficient. They are able to capture electrons on their way to the anode of a drift cell, nevertheless their attachment coefficient stays small compared to other

molecules such as $Oxygen$ or water. The later two, having a high electronegativity, and being a component of the air, usually pollute the counting gas mixture of a detector, and capture the drift electrons, reducing the measured pulse height and consequently the resolution of the detector. The attachment coefficient is, however, not constant, and it varies with the electron energy and consequently with the electric field. Figure 4.5 shows the dependence of the attachment coefficient of the gas mixture used in the HADES drift chambers, for different percentages of O_2 and H_2O pollution on the reduced electric field.

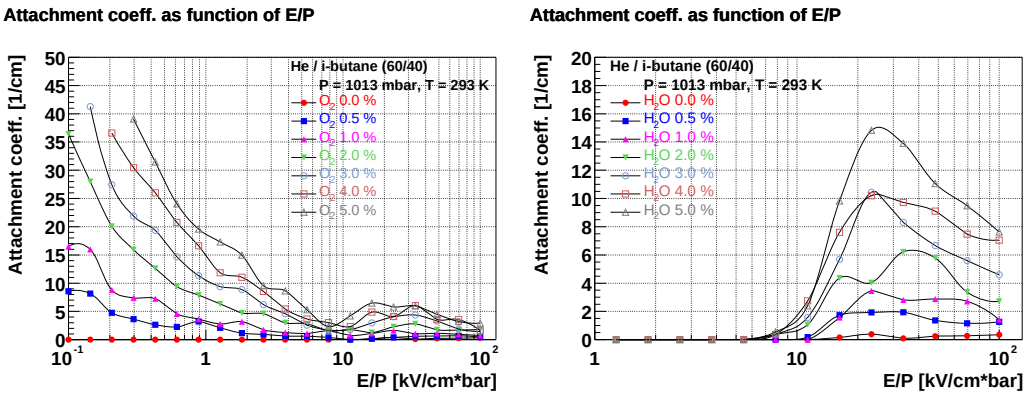

(a) (b)

Figure 4.5: Attachment coefficient as a function of the reduced electric field for: (a) different O_2 concentrations, (b) different H_2O concentrations, in a (60/40) $He/i-butane$ mixture.

The behavior of both types of contaminations is totaly different. While the attachment coefficient of water is almost negligible for reduced fields below 9 $kV/cm \cdot bar$, that of oxygen is considerably high up to that value of the reduced field. Oxygen captures drift electrons far from the sense wire of a drift cell, where the electric field value is relatively moderate, and herby reduces the number of electrons which reaches the gas multiplication region. This reduces the pulse height and of course the resolution of the detector. Therefore, it is mandatory to prevent oxygen contamination of the counting gas. In contrast to oxygen, the water vapor in the counting gas can be used to help ensuring a stable operation of the detector. The attachment coefficient for water is negligible for fields that are typical in a drift cell far from the sense wire. Only for the field values usually present near the sense wire, where the avalanche multiplication takes place, the attachment coefficient of water has a high value so that it can capture electrons. By capturing electrons in the avalanche region, the water vapor can prevent the spark breakdown of the detector. The process of avalanche multiplication and relevant aspects will be dis-

cussed in section 4.2.5.
If c is the fraction of electronegative pollutant in the gas, λ and u the electron mean free path and instant velocity, and W and h the drift velocity and the attachment coefficient, respectively, the mean free path for electron capture λ_c is then given by:

$$\frac{1}{\lambda_c} = \frac{huc}{\lambda W} \tag{4.22}$$

or, substituting from equation 4.19 we get:

$$\lambda_c = \sqrt{\frac{m}{2\varepsilon}} \frac{W}{Nhc\sigma(\varepsilon)} \tag{4.23}$$

and the number of electrons n out of n_0 remaining after drifting along a distance x is given by:

$$n = n_0 e^{-x/\lambda_c} \tag{4.24}$$

4.2.5 Avalanche multiplication

The process of avalanche multiplication is essential for obtaining a detectable pulse in a gas detector. As calculated in section 4.1.3 the total number of electrons produced by a minimum ionizing particle in a plane IV drift cell is about 83 electrons. The capacitance of this cell is in the order of 8.85 pF (see section 8). If the electrons are collected at the sense wire, they will produce a signal of height V given by:

$$V = \frac{ne}{C} = 1.5 \quad \mu V \tag{4.25}$$

where n is the number of electrons, e is the electron charge, and C is the capacitance of the cell. This signal is far below any possibility of detection. The avalanche multiplication however, multiplies the number of electrons by a factor of $10^4 - 10^6$ making it possible to detect the signal and register the particle as will be described below.
As long as the electric field acting on the drift electrons is relatively moderate, the electrons will mainly experience non-ionizing collisions with the gas atoms along their drift way. If the electric field is high enough, electrons can get enough energy between two collisions to be able to ionize atoms and molecules of the gas. While the electron ionizes a molecule of the gas and continues its trip, the new electron produced at the last ionizing collision starts also to drift under the influence of the field. Again, both electrons can further ionize molecules of the gas producing two other electrons, and soon the number of electrons released by the ionizing particle is multiplied by many orders of magnitude. This is the main

concept of the avalanche multiplication, and the collected signal reaches then reasonable detectable values.
The mean free path of ionization is defined as the average distance an electron travels before being involved in an ionizing collision. The inverse of the mean free path of ionization is called the first Townsend coefficient α, and it represents the number of ion pairs produced per unit length of drift. Figure 4.6 shows the variation of α with the reduced field for different $He/i-butane$ mixtures.

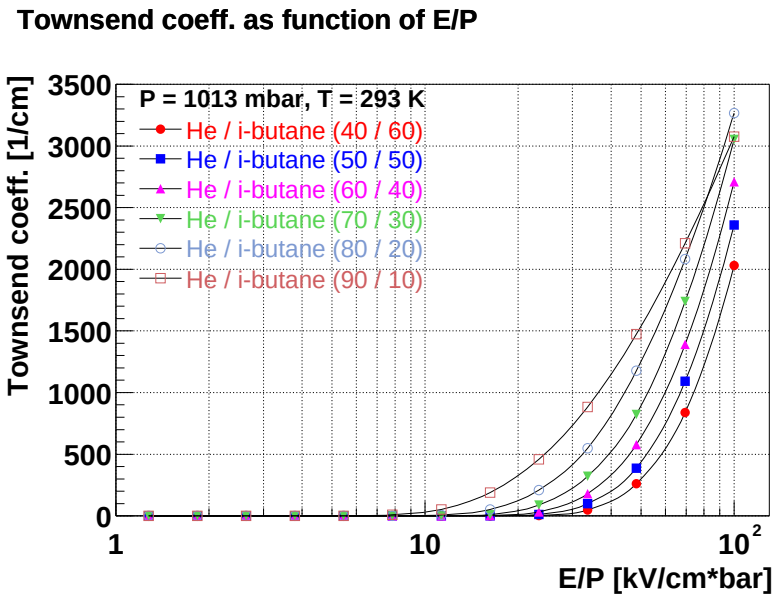

Figure 4.6: First Townsend coefficient as a function of the reduced field for different $He/i-butane$ mixtures.

In a non-uniform electric field $\alpha = \alpha(x)$, and if n_1 is the number of electrons at position x_1, the number of electrons n_2 and the multiplication M at position x_2 is given by:

$$M = \frac{n_2}{n_1} = exp\left(\int_{x_1}^{x_2} \alpha(x)dx\right) \tag{4.26}$$

The difference in the drift velocity between ions and electrons is about three orders of magnitude. Electrons created in the avalanche process instantly leave the ions behind. At a given instant, they are all situated in the front of a drop-like distribution of charges, with a tail of positive ions, decreasing in number and lateral extension. Half of the ions are in the front part of the drop, since they have just been produced in the last mean free path for ionization.

The multiplication factor cannot be increased arbitrarily. Secondary processes, like photon emission inducing the generation of avalanches spread over the gas volume, and space-charge deformation of the electric field (which is strongly increased near the front of the avalanche), eventually result in a spark breakdown.

4.3 Principles of operation in a drift chamber

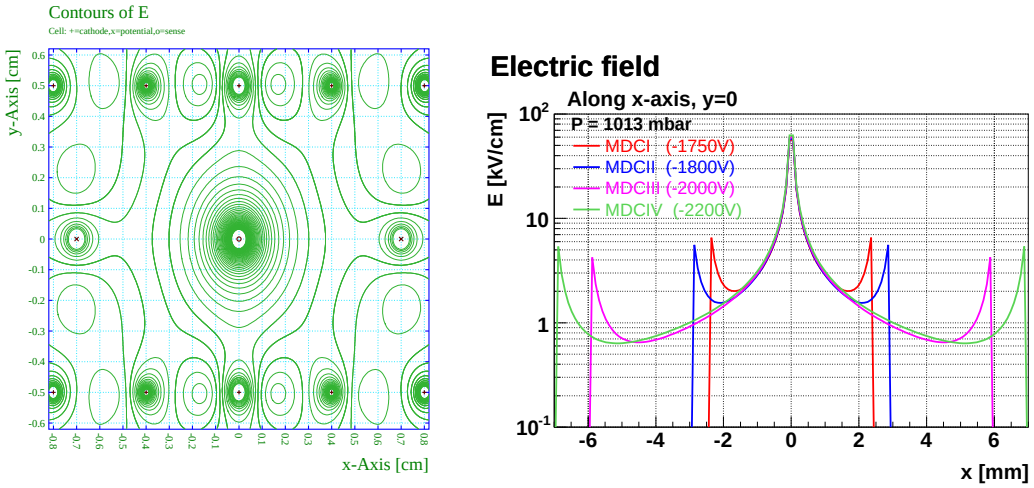

(a) (b)

Figure 4.7: Contour of the electric field in the drift cell for MDC-IV. The cathode- and field wires are set to a negative potential of -2200 V. Contour lines in (a) are in steps of $\Delta E = 200\ V/cm$. (b) Electric field through the middle of the different drift cells in x-direction. The potential applied on the cathode and field wires equals: -1750 V (MDC-I), -1800 V (MDC-II), -2000 V (MDC-III) and -2200 V (MDC-IV).

Figure 4.7.(b) shows the value of the electric field along the x-axis of an MDC-IV drift cell through the middle of the cell. As seen in figure 4.6, the ionization cross section is negligible for values of E/P below 30 $kV/cm \cdot bar$ for the gas mixture used in the HADES drift chambers. Only when the reduced field comes above this value, ionization collisions can have a considerable probability and the avalanche multiplication can take place. Referring to figure 4.7.(b), it is clear that those field values, necessary for the avalanche process to take place, exist only a few tens of micrometers near the sense wire. Over the whole drift cell, the electric field is so moderate, such that it does only make the primary and

secondary electrons drift towards the sense wire, and the ions towards the potential wires. Only very close to the sense wire, the field value becomes so high, that the avalanche multiplication starts, so that one, at the end, gets a sufficient number of electrons collected at the sense wire, proportional to the original number of electrons, and enough to produce a detectable signal. The design of the cell, mainly limited by mechanical constrains, is chosen such that the drift velocity away from the sense wire doesn't vary so much, so that one can calculate the position of the particle track through the cell by measuring the drift time of the electrons.

The detected signal, negative on the sense wire and positive on the potential wire, results from the change in the energy of the system due to the movement of charges. The electrons, half of them being created in one mean free path from the sense wire, contribute only to a small part of the signal. The main part of the signal is induced by the slow movement of the avalanche ions from the neighborhood of the sense wire, across half of the drift cell, to the potential wires.

4.3.1 Counting gas properties

As mentioned before, the avalanche process is the main basis of the operation of a gas detector. Referring to figure 4.6, the ionization cross section is higher, the higher the He concentration in the $He/i-butane$ mixture, used in the HADES drift chamber. A polyatomic molecule, like $i-butane$ has many non-ionizing energy dissipation modes (rotational and vibrational) compared to a noble gas like He. Therefore, the avalanche process can take place in a noble gas at much lower fields than in a complex molecule, and hence the noble gas is chosen as the main component of the counting gas in a drift chamber. The choice of He instead of Ar in the HADES drift chambers, helps fulfilling the *low-mass* concept in the chambers. However, filling the drift chamber with a noble gas only will not allow a stable operation. During the avalanche process, excited and ionized atoms are created, which, for the case of a noble gas, can return to the ground state only through photon emission. The energy of the emitted photon will be above the ionization potential of the metal constituting the potential wires. A photoelectron can be released from the potential wires, and initiate a new avalanche very soon after the primary. Also, the positive ions migrate to the potential wires, where they are neutralized extracting an electron. The balance of energy is either radiated as a photon, or by secondary emission. Both processes lead to a new avalanche, and a permanent regime of discharge is created, called *self-sustained* current.

The polyatomic molecules, on the other hand, can absorb the photons emitted by the excited noble gas atoms, as it has many rotational and vibrational energy

states, which covers a wide range of the photon energy. Such molecules are called *quenchers*. They dissipate the excess energy either by elastic collisions, or by dissociation into simpler radicals. Also when neutralizing at the potential wires, the secondary emission is very unlikely. Because of their lower ionization potential resulting in a very efficient ion exchange (see section 4.2.2), the addition of even small amounts of a polyatomic molecule to a noble gas, does considerably change the drift properties and the operation of the chamber.

The addition of only small quantities of electronegative gases allows one to obtain the highest possible multiplication. The electronegative gases capture free electrons forming negative ions that cannot produce avalanches. If the mean free path for capture is shorter than the distances between the sense and potential wires, any electron librated at the potential wires by the processes described before, is most probably captured before it reaches the avalanche region. However, to preserve detection efficiency, only a small amount of electronegative gases can be added to the mixture, otherwise the primary electrons will be absorbed.

Chapter 5

Drift time measurement

The drift chambers of the HADES experiment are used to trace the charged particles emitted in heavy ion reactions into the acceptance of the spectrometer. The particles' trajectories can be reconstructed using the information of the positions of the drift cells which were crossed by a certain particle and the distance to the sense wire at which the particle passed through the individual cell. This distance is obtained through the measurement of the drift time of the electrons released by the passage of the particle through the cell to the sense wire. The drift times can be measured only relative to another external time signal *(trigger)*. This time signal is called the *common-stop* (CMS), and its concept will be described in details in section 5.1. The raw data registered by the TDC's of the drift chambers readout electronics have to be converted into physical drift times of the drifting electrons released by charged particles traversing the chamber. For this, one needs to understand the principle of the measurement in the drift chambers.
Two electronic chips take part in the drift time measurement in a drift cell, the 8-channel **A**mplifier **S**haper **D**iscriminator chip (ASD8) [New93], and the 8-channel **T**ime to **D**igital **C**onverter chip (TDC). The schematic sequence of the drift time measurement is shown in figure 5.1.

For the drift time measurement, the following holds:

- The passage of ionizing particles through the chamber releases electrons, which drift to the readout wire (signal wire). The drift time is the time which the released electrons need to reach the wire.

- The drift time measurement starts when the signal induced on the wire arrives at the TDC. Hence, the start of the measurement is not a unique function of the time instant of the reaction in the target.

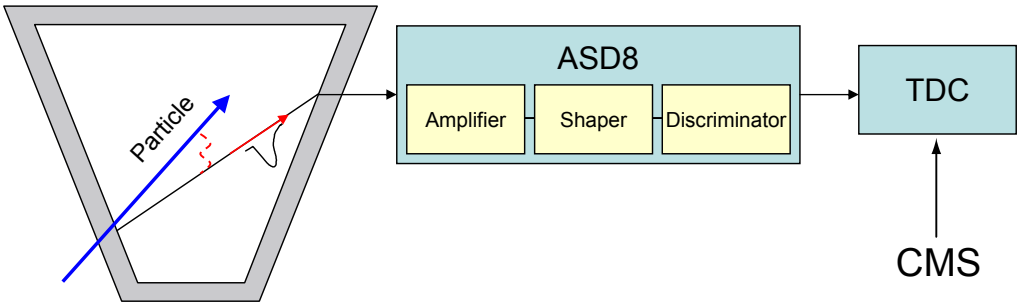

Figure 5.1: Schematic representation of the drift time measurement in the MDC's. The signal induced by an ionizing particle propagates to the readout electronics. In the analog part of the electronics (the ASD8), this signal is amplified, shaped and digitalized. The digital output signal of the ASD8 starts the measurement in the TDC, and the measurement is stopped by the *common-stop* signal (CMS).

- The TDC measurement is *self-triggered*. The measurement starts after the drift of the electrons is already finished.
- Each particle needs a different time-of-flight to reach the particular drift cell which results in a delay added to the measured drift time.
- The induced signal has to propagate along the signal wire to the readout electronics which causes an additional delay.
- The drift time measurement does not start immediately with the arrival of the first electron at the readout electronics. Another delay is added since the analog signal has to overcome a given threshold in the ASD8 to start the measurement.
- The time measurement of all channels is stopped simultaneously through an external signal (CMS) which has a fixed correlation with the reaction instant.

5.1 Common stop (CMS) concept

The following trigger scheme is implemented in the HADES-experiment:
The point of time of a heavy ion reaction in the target cannot be measured directly. Instead of that, a high precision ($\Delta \approx 50\ ps$) time signal is generated when a beam particle passes through the START detector. The decision whether

a reaction took place in the target, and is accepted for the data acquisition follows in different stages depending on the configuration of the event selection. The data of the START and VETO detectors as well as, of the TOF and TOFino/SHOWER detectors take part in this decision.
The START detector signal is then delayed and sent to the drift chambers as a signal to stop the drift time measurement in the TDC's (CMS). Hence, the TDC measures the difference between the point of time when the amplified shaped drift electrons signal overcomes the ASD8 threshold (*self triggered* start) and the delayed START detector signal (CMS). In order to retrieve the drift times of the released drift electrons from the times measured by the TDC, the following two steps have to be carried out:

- The measured TDC times $(unit = TDC\ channel)$ have to be converted into physical times $(unit = ns)$. The calibration coefficient $(unit = ns/channel)$ of each individual TDC channel must be determined. This is done through the internal calibration procedure as described in chapter 6.
- The point of time of the start of the electron drift has to be reconstructed in order to calculate the distance between the particle trajectory and the readout wire. The methods for determining the start of the drift time measurement are described in details in chapters 7 and 8.

Chapter 6

Calibration coefficient of the TDC

The raw drift times measured by the TDC are in units of $TDC - channel$. These values have to be converted into physical times in order to be used for the determination of the particle trajectory inside the chamber. Therefore, the determination of a calibration coefficient for each TDC is necessary. Assuming a linear relation between the elapsed time and the recorded TDC-channel, the calibration coefficient of a TDC is a constant value which has the units of $(ns/channel)$. This value varies from one TDC channel to another depending on its installation position, the amount of data flowing through it, and also manufacture tolerances. Two factors affect the value of the calibration coefficient of a specific TDC, namely, the temperature and the bias voltage. Both are discussed in the next two sections.

6.1 Dependence on temperature

The TDC calibration coefficients increase with increasing temperature by about $(0.16\ \%/^{\circ}C)$[Wüs98]. This value is important because of the following two facts:

- Depending on its position and cooling conditions, and the data load on the TDC chip, the temperature difference can reach up to $20^{\circ}C$ between the starting room temperature in the cave ($\sim 20^{\circ}C$) and the equilibrium temperature of the chip ($\sim 30^{\circ}C - 40^{\circ}C$) after data taking for several hours.

- The measured drift times lie typically around 1600 TDC-channels. This value has to be multiplied by the calibration coefficient in order to obtain the physical time ($\sim 800\ ns$). A change of only 0.3% results in a systematic error in the drift time of about 2.4 ns.

After reaching the equilibrium temperature, the TDC calibration coefficient does not change considerably. It can be taken as a constant as long as the experiment is running. Using coefficients determined at equilibrium temperature reduces the systematic error in the drift time measurement.

6.2 Dependence on bias voltage

Another factor which can change the value of the calibration coefficient of a given TDC is the bias voltage. A reduction of the bias voltage decreases the proportionality between the TDC channel counts and the time. The calibration coefficient increases in that case by about $0.022\,\%/mV$[Wüs98].
A decrease in the bias voltage may result from a high data load on the system. During the internal calibration process (see section 6.3) and during a beam spill, such a high load can be exerted on the system, which can lead to a reduction of the supply voltage and thereby change the TDC calibration coefficient. For this reason the internal calibration is performed for only a small part of the TDC's at the same time. Thereby the load on the voltage supply systems is comparable to the situation during data taking.

6.3 Internal calibration

For the determination of the calibration coefficient, the internal calibration function provided by the TDC is utilized. Using a special trigger (internal calibration trigger) a clock is set to consecutively send 4 square pulses of 400 ns periodic time and $50\,\%$ duty cycle to the channels of the TDC chip (see figure 6.1). The clock is rather precise, and hence one has 6 consequent edges with 200 ns separation. The leading edge of the fourth pulse is used instead of the common stop to end the measurement [Zum98]. The TDC measures the times of the six edges and, assuming a linear behavior of the TDC, one can fit the measured times using a linear regression and obtain the calibration coefficient as the fit result.

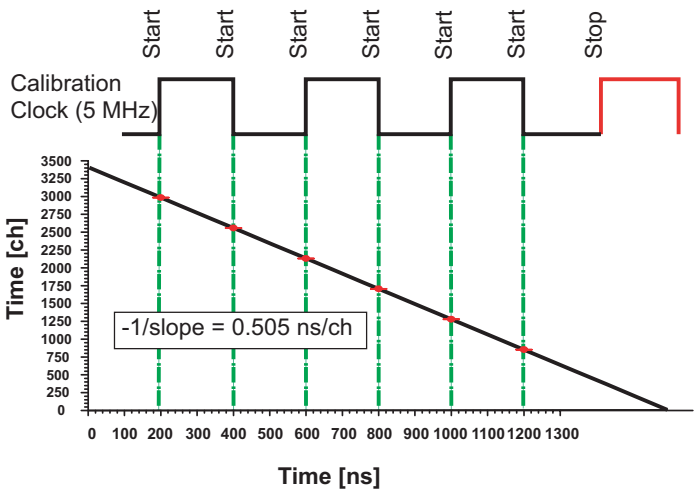

Figure 6.1: Principle of the internal calibration of the TDC [Zum01]. The TDC measures three rising and three falling equidistant edges ($\Delta t = 200\ ns$). Using a linear regression, the TDC calibration coefficient is calculated from the 6 measurements.

6.3.1 Offline calibration

Two approaches are used in order to collect the internal calibration data; the first of them is called the *offline* calibration. In this method, the internal calibration data are collected before and after the experiment. No other type of data is taken during the calibration. The calibration data are taken at a constant trigger rate.
Due to the limited capacity of the ROC buffer, calibrating all channels simultaneously is not possible. Instead of that, using a special routine (the so-called *rotating mask*), only one channel out of the 8 channels of each TDC chip is calibrated in an internal calibration event. The routine changes the TDC channel to be calibrated each 10 internal calibration events. The amount of data in each event is reduced to the eighth, and the load on the voltage supply systems as well.
To obtain comparable calibration coefficients as during the experiment, the internal calibration data are taken for a long period of time in order to allow for the electronics to reach their equilibrium temperature. A pronounced warming up phase can be observed through the internal calibration process. Calibration coefficients calculated during the warm-up phase have an error larger than $1\ \%$, while those determined after the system has reached its final temperature show an error of about $0.1\ \%$ [Mar05]. As mentioned in section 6.1, an error of $1\ \%$ in the calibration coefficient leads to a systematic error of about 8 ns which is far

beyond the acceptable limit. Whereas an error of $0.1\,\%$ is still feasible taking into consideration the resolution of the drift time measurement itself (1-3 ns).
After accumulating enough internal calibration data at the saturation temperature, the distribution of the obtained coefficients for each individual channel is fitted with a gaussian. The mean value and the standard deviation of the distribution, and their errors are retrieved from the fit. The mean value is taken as the channel calibration coefficient.

6.3.2 Online calibration

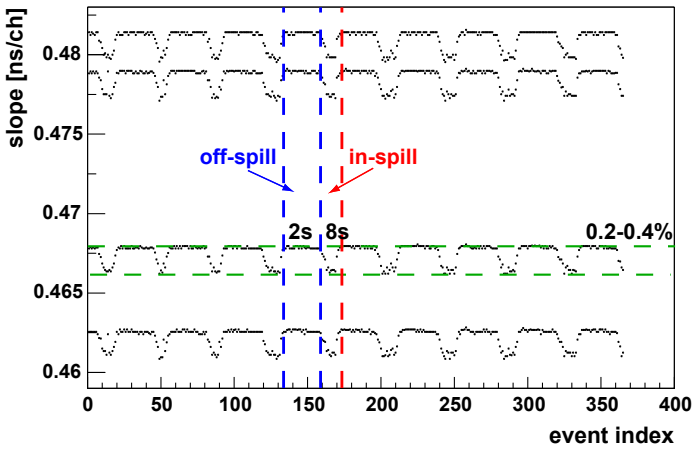

Figure 6.2: Variation of the calibration coefficient of four selected channels in the online calibration as a function of the event number. The time intervals of ($8\ s$) during the beam spill, and ($2\ s$) when no beam is available are marked (red/blue). The calibration trigger has a lower priority than the real events trigger, thus reducing the number of calibration events per unit time for *in spill* periods compared with *off spill* periods.

While the offline calibration is performed before and after an experiment, the *online* calibration data are taken during the experiment. This assures that the calculated calibration coefficients are exactly the same as during the data production. The internal calibration trigger is set to a few Hz, so that it does not hinder the collection of reaction data. The calibration coefficient as a function of time exhibit a significant *off spill/in spill* structure (see figure 6.2). This demonstrates the effect of the changing load and temperature of the readout electronics due to the varying amount of data taken. It also shows the advantage of the online calibration in comparison to the offline one. With the online calibration, one can

trace the changes in the conditions of the system, and even create different sets of calibration coefficients for different periods of the beam time.

The same procedure for calculating the final calibration coefficients in the offline calibration method is used in the case of online calibration. The distributions of the calibration coefficients are fitted with a gaussian to obtain the mean value and the error of the coefficients. During the experiment, the internal calibration trigger has a lower priority than the normal physics event, hence, the number of calibration events during the spill brake is larger than during the spill. Therefore, the *off spill* calibration parameters contribute more to the fit result than the *in spill* ones. Their difference is in the range of $0.2\,\% - 0.4\,\%$, which results in an error in the drift time of about $1.6 - 3.2\,ns$ [Zum05].

6.4 Calibration of external pulser data

For the external pulser data (see chapter 8) the method of online calibration has been utilized. The effect of *off spill/in spill* variation was avoided by taking the data under constant load.
Although all files were taken after the system has reached stable temperature conditions, some variation in the coefficients between different calibration events are still present. Since the files are taken only for short times, the amount of calibration data is not enough to allow the gaussian fit to always converge to the mean value. Figure 6.3 shows an example of a channel where the mean value of the gaussian fit is far away from the determined coefficient range. As the files are taken under stable conditions, the variations in the coefficients are usually too small, to affect the quality of the data. Figure 6.4 shows the distribution of the root-mean-square values of the calibration coefficient spectra for all TDC channels. The mean value of the distribution is less than 0.0003 ns/ch. The pulser data lie usually between channel 1000 to 1200 of the TDC. A coefficient error of 0.0003 ns/ch leads to a systematic error in the measured pulse time of less than 0.4 ns which is much low below the accuracy of the method. Therefore, for the pulser files, the mean value of the calibration coefficient distribution was taken instead of the fit result. Figure 6.5 shows the distribution of the difference in the calculated calibration coefficient value between the gaussian fit result and the mean value. The mean value of the difference lies at 0.0024 ns which corresponds to a systematic error in the pulser times of about 2.9 ns. Figure 6.6 shows the distribution of the calibration coefficient values of all TDC channels of the MDC system.

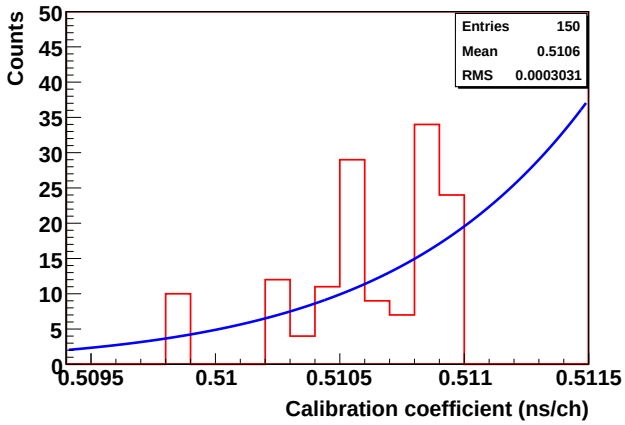

Figure 6.3: Distribution of the determined calibration coefficient of one TDC channel. The mean value of the distribution is 0.5106 (ns/ch) and the root-mean-square value is 0.0003 (ns/ch). The blue line represents a failed gaussian fit to the distribution. The mean value of the gaussian function lie at 0.5232 (ns/ch) far away from the mean value.

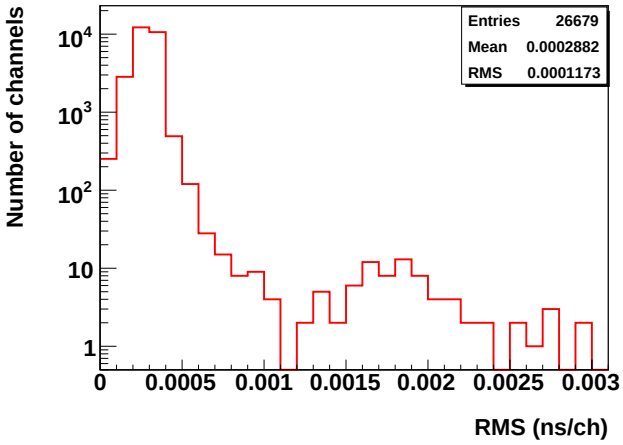

Figure 6.4: Distribution of the RMS value of the TDC calibration coefficient spectrum for all TDC channels.

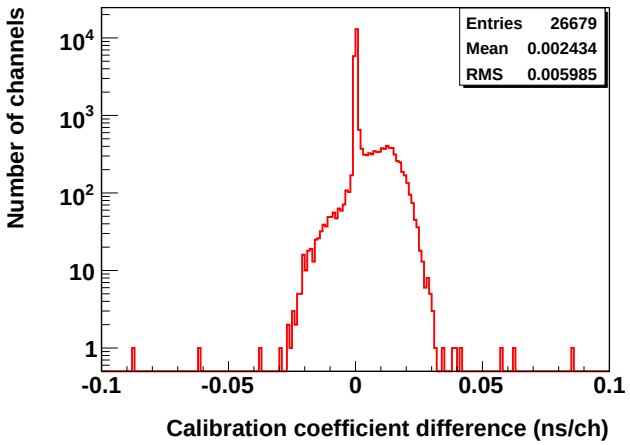

Figure 6.5: Distribution of the difference of the calculated calibration coefficient between the gaussian fit result and the mean value of the coefficient spectrum for each TDC channel.

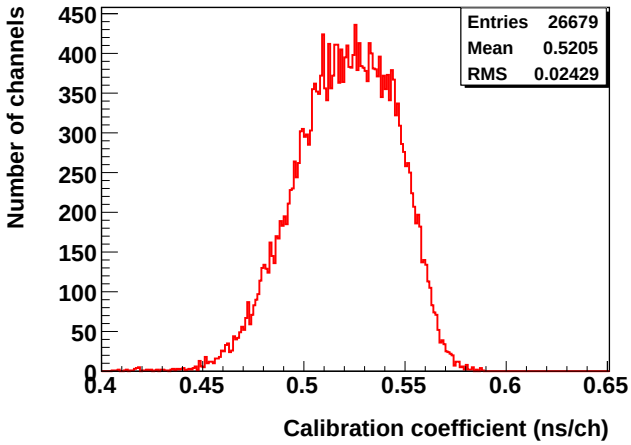

Figure 6.6: Distribution of the TDC calibration coefficient of all TDC channels.

Chapter 7

Channel calibration constant

After calculating the TDC calibration coefficient using the internal calibration, the calibration constant of the corresponding TDC channel has to be determined. The calibration constant defines the start point of the drift time measurement. The drift time is calculated using the following formula:

$$t_{drift} = [t_{offset} - t_{raw} \cdot slope_{TDC}] - t_{wire}, \tag{7.1}$$

$$\begin{aligned} t_{offset} &\text{ - Calibration constant } [ns] \\ t_{raw} &\text{ - TDC-time } [channels] \\ slope_{TDC} &\text{ - TDC-calibration coefficient } [ns/channel] \\ t_{wire} &\text{ - Propagation time of the signal on the signal wire } [ns] \end{aligned} \tag{7.2}$$

The propagation time can only be calculated after the particle trajectory has been reconstructed. The only variable which remains to be determined is the calibration constant. For the determination of the constant two different methods are applied. In this chapter the determination of the calibration constant using experiment data will be described. The other method will be discussed in detail in the chapters 8, 9, and 11.

The determination of the calibration constants using experiment data is based on the idea that if the number of measured tracks traversing a drift cell is large enough, the point of origin of the measurement, *i.e.* the calibration constant, can be deduced from the drift time spectrum. It is assumed that, out of a sufficiently large number of tracks, a considerable part of them originates from particles which

crossed the drift cell close to the signal wire. For such tracks, the drift time is essentially negligible and their drift time, as registered by the TDC, defines the point of origin of the drift time measurement.

After the reconstruction of a particle trajectory through a chamber the distance which the induced signal had to propagate along the signal wire to the readout electronics is known. Hence, the propagation time can be calculated and subtracted from the measured drift time. Nevertheless, the calculated constants still contain systematic differences between the different chamber planes and between different regions inside each chamber. These differences arise mainly from the times-of-flight needed by the particles to reach the corresponding drift cell.

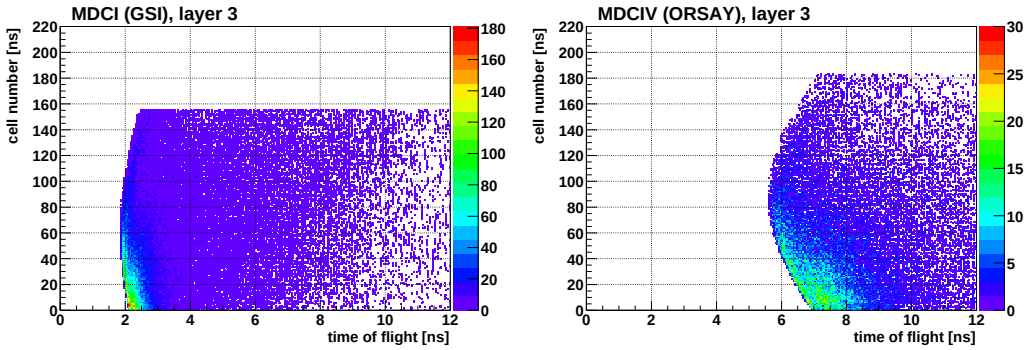

(a) (b)

Figure 7.1: Simulated time-of-flight distribution of particles crossing the first 0° layer of (a) a plane I chamber and (b) a plane IV chamber, in $C + C$ collisions at a beam energy of 2 $AGeV$.

Figure 7.1 shows the distribution of the time-of-flight needed by the particles produced in simulated $C + C$ collisions at 2 $AGeV$ to reach the drift cells of a given layer in the first and last drift chamber planes. Between the two chambers, the difference in the minimum time-of-flight is about 3.5-5 ns. Furthermore, throughout the same layer, differences in the minimum time-of-flight of up to 1.5 ns can be observed between the different drift cells.

The cell number in 0° layer is directly correlated with the polar angle. Cells at low polar angles correspond to small numbers. Looking at figure 7.1, these cells experience a higher rate of particles as compared with those at high polar angles. Consequently, the statistical error of the deduced calibration constants rises with increasing cell number. For the same reason, the noise impact in the determination of the calibration constants increases leading to a bigger systematic error at high polar angles.

To reduce the error arising from the noise background, only the measurements of the drift times which were used to reconstruct particle trajectories are considered when determining the offsets. Measurements out of the physical range of drift times are discriminated *(Time1 cut)*. Another cut is applied to the width of the measured signal, to suppress noise measurements with typical small widths *(Time2-Time1 cut)*.

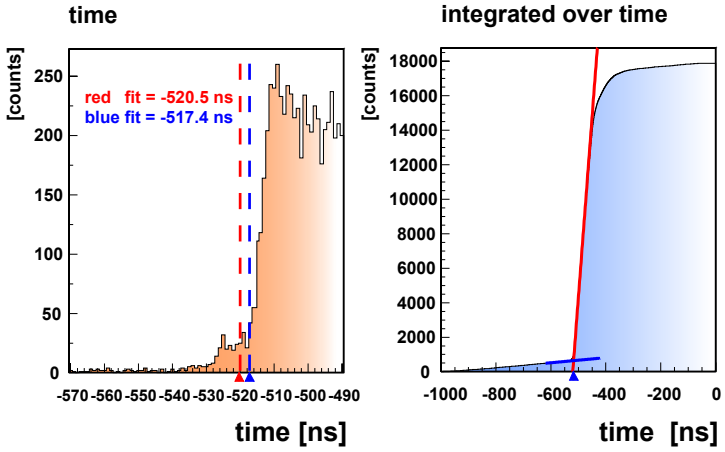

Figure 7.2: Procedure of determining the calibration constant of a drift cell. The drift time spectrum *(left)* is integrated *(right)*. The constant is determined from the intersection of the two straight lines fitting the signal (red) and the noise (blue).

The following method was developed to determine the calibration constants:

- The track reconstruction software spatially correlates the drift cells belonging to the same trajectory. Only these drift cells are used for the determination of the calibration constant [Mar05].
- The selected measurements must fulfill the conditions of the *Time1* and *Time2-Time1* cuts.
- The propagation time of the signal on the signal wire to the readout electronics is subtracted from the drift time. The speed of propagation of the signal is $0.25\ m/ns$.
- A drift time spectrum for each drift cell is filled with measurements of an appropriate number of events.
- The spectrum of each individual drift cell is then integrated. The integrated spectrum rises steeply at the beginning of the drift time spectrum.

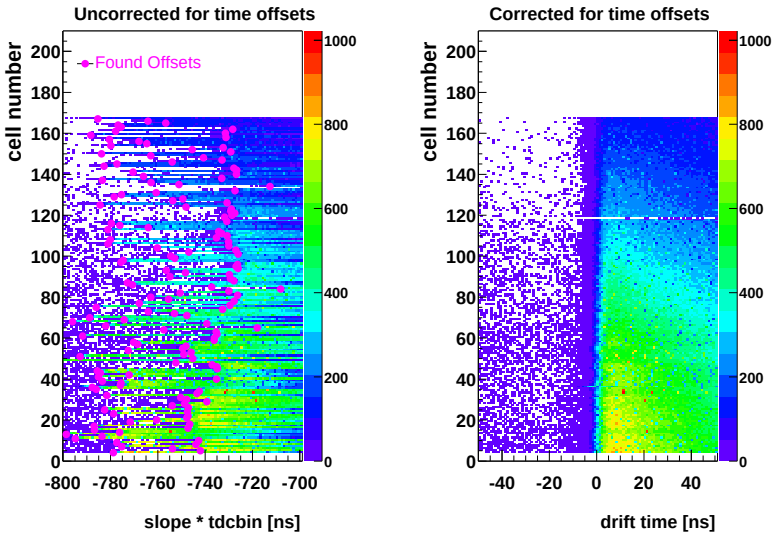

Figure 7.3: Drift times as a function of the drift cell number of one 0° layer of a plane III chamber; before (left) and after the calibration (right). The magenta points on the left picture indicate the position of the determined constants

- The rising edge of the integrated spectrum is fitted by a first order polynomial and the intersection with the abscissa is calculated to determine the zero point of the drift time measurement.
- In a second step, the part of the spectrum before the determined zero point is fitted using a first order polynomial. This fit describes the noise contribution in the drift time spectrum.
- Finally, the calibration constants are calculated from the intersection of the straight lines obtained from the two fits described above. The calibration constant errors are estimated from the parameters of the two fits.

Figure 7.3 demonstrates the result of the calibration procedure. The left picture shows the spectrum of drift times for a given layer of a plane III chamber as a function of the cell number. The start point of the physical arrival times in each cell scatters throughout the layer within 100 ns. The magenta colored points indicate the determined calibration constants. After calibrating the picture to the right is obtained where all physical times start have the same point of origin. A more detailed description of the method and results can be reviewed in [Mar05].

Chapter 8

External pulser

As an alternative method to the determination of the MDC calibration constants using the experiment data (see chapter 7), the calibration using an external pulse generator – the so called *pulser* – has been considered. As described in chapter 3, each field/cathode layer is supplied individually with high voltage through the so called *HV-Box*, which, in addition, filters out high frequencies in order to ensure a stable and noiseless operation of the chamber. The position of the HV-Box on the chamber frame varies from one plane to another. Figure 8.1 represents a schematic diagram of a HV-Box with a pulser input.

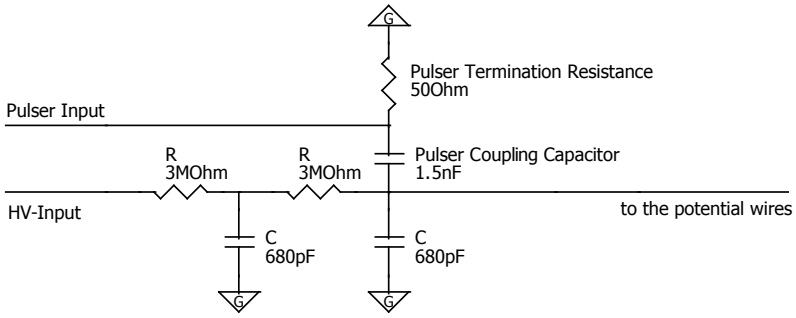

Figure 8.1: Schematic diagram of a high voltage box with a pulser input. The HV is fed through the RC filter to the field/cathode wires of the chamber. The pulser signal is capacitively coupled to the wires behind the filter.

The calibration pulse sent to the pulser input is capacitively coupled to the potential wires of the corresponding layer. The pulse propagates along the HV distribution lines on the inner chamber frame to the potential wires of the layer. The capacitance of the signal wire in a drift cell can be approximated by [Sau77]:

$$C = \frac{2\pi\epsilon_0}{(\pi\ell/s) - \ln(2\pi a/s)} \tag{8.1}$$

where

- C is the capacitance per unit length
- ϵ_0 is the dielectric constant of the counting gas $\simeq 8.85\ pF/m$
- a is the radius of the signal wire
- ℓ is the distance between the signal and cathode wires
- s is the distance between the signal and field wires

Substituting with dimensions of a plane III chamber, one obtains a capacitance of about 8.36 pF/m. Through this capacitance, the pulser signal on the potential wires induces a signal on the neighboring signal wires. The induced signal propagates along the wire, until it reaches the readout electronics. The readout electronics amplifies, shapes, and discriminates the signal. The logical output signal starts the time measurement process in the corresponding TDC channel.

8.1 Concept of the method

The concept of determining the MDC calibration constants using the external pulser is explained as follows. Since all signals on the signal wires originate from the same pulse, they are time correlated. After subtracting the time they need to propagate from the HV-box to the readout electronics of each signal wire, the differences in their arrival times as registered by the TDC's are a measure of the relative time constants of the wires (i.e. of the respective electronic channels).
Figure 8.2 shows the distorted input signal at the input of the high voltage box and the signal induced on a readout wire. Both are simulated using a spice program [5sp05]. The amplitude of the induced signal is less than 0.5 % of the input amplitude. In addition to the oscillations induced by the circuitry of the high voltage box and the wires of the chamber as shown in figure 8.2.(b) we expect reflections caused by the missing termination of the potential wires. A real signal on the sense wire is reproduced in figure 8.3.(a). It is a superposition of the phenomena described above and all other possible effects which were not accounted for in the simulation.

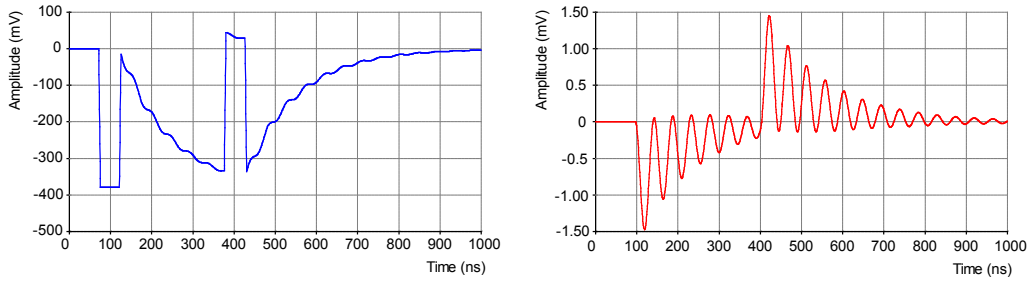

(a) (b)

Figure 8.2: (a) Input pulse: A gate signal of 2.5 ns rise time and 300 ns width is partially distorted because of the impedance and oscillations introduced by the high voltage box and the wires of the chamber. (b) Induced signal on a signal wire: the amplitude is less than 0.5 $\%$ of the input.

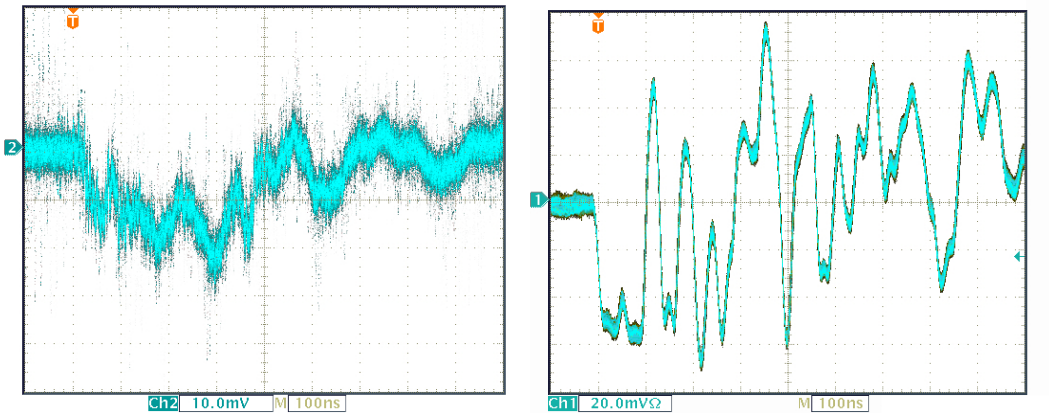

(a) (b)

Figure 8.3: (a) Pulser signal induced on a signal wire of a plane IV chamber: small amplitude (30 mV) superimposed by reflections. (b) ASD8 analog output: the amplified shaped pulser signal on a signal wire at the output of the shaper of the ASD8. The first leading edge in (b) corresponds to the first leading edge in (a) and is supposed to trigger the discriminator.

8.2 Determining the calibration constants

For determining the calibration constants of all MDC's a pulser signal is sent to the HV-Box of each chamber. 500 ns later, a CMS signal is sent to the readout system (see chapter 5). The difference in time between the arrival of the pulse at the input of a particular ASD8 channel and the arrival of the CMS at the corresponding TDC channel is recorded. Repeating this process, a statistical distribution of the registered times of the signal relative to the CMS is obtained. The mean value of the distribution provides – after some corrections – the value of the calibration constant of the corresponding channel. This scheme applies to all signal wires.

As in the case of the internal calibration, only one eighth of the readout channels is readout in each event in order to reduce the amount of data to the capacity of the read-out controller buffer (see chapter 6.3).

The following steps summarize the procedure of determining the time constants using the external pulser method:

- The pulser signals are sent to the chambers at a rate of 1 kHz and the data are collected for about 3 $minutes$. The internal calibration is carried out in parallel at a rate of 10 Hz.
- The internal calibration data in the recorded data file are analyzed, and the values of the TDC calibration coefficients are written to a parameter file.
- Using the obtained TDC calibration coefficient, the collected pulser data are read and converted from the raw TDC time format, to physical times in nanoseconds. For each wire, the spectrum of the registered signal times is filled (see figure 8.4.(a)).
- A peak finding algorithm determines the position of the peak in the time spectrum, which corresponds to the relative calibration constant of the considered channel (see figure 8.4.(b)).
- The mean value and the RMS of the distribution are written to a parameter file. Figure 8.4.(c) shows the spectrum of the RMS values of all channels.
- Table 8.1 summarizes the result of the external pulser measurements concerning the number of calibrated channels and the width of the spectrum.

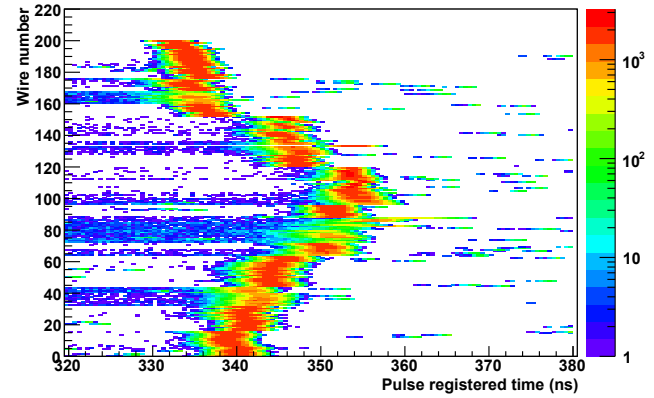

(a)

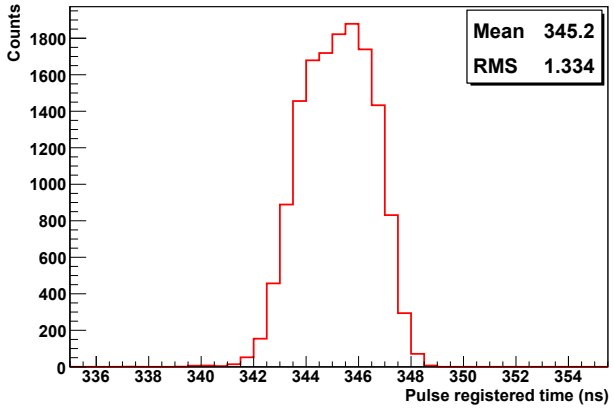

(b)

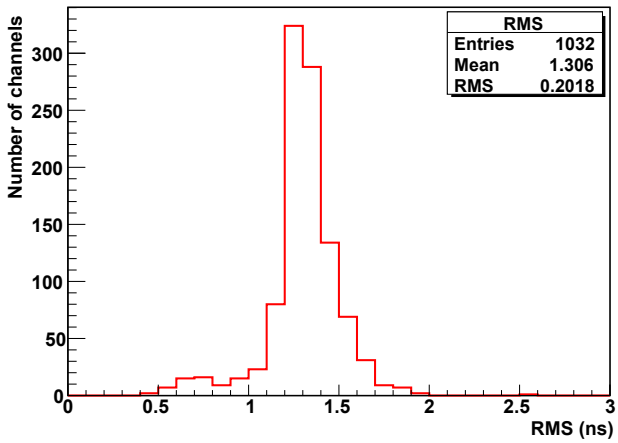

(c)

Figure 8.4: (a) Pulser time spectrum for one plane IV layer. The abscissa represents the calibrated times. The ordinate indicates the wire number. (b) A projection of the two-dimensional histogram in (a) on the abscissa for one wire. (c) Distribution of the RMS values of the pulser spectrum for all channels.

External pulser method	
Total number of wires	1168
Wires having no counts	21
Wires with more than one peak	115
Width of the peak	1-2 ns
Data based method	
Non calibrated wires	74
Wires having a default calibration value	79
Accuracy of the method	NA

Table 8.1: Results of the external pulser and the data based methods.

The mean values of the time spectrum do not represent the final values of the calibration constant. They have to be corrected for the propagation time differences between the different channels as will be discussed in detail in chapter 9. Furthermore, and since the timing of the CMS signal relative to the pulser signal is arbitrary, a global correction constant for all channels is used. The global correction constant is determined by an iterative process as described in chapter 11 section 11.2.

Chapter 9

Signal propagation time

In the pulser calibration method an electric signal is coupled to the HV distribution system of a chamber through its HV-box. This box has a certain position on the chamber frame. From that position the signal has to propagate along the various wires of the chamber to the readout electronics of each individual signal wire. A precise determination of the propagation time is needed to correct the calibration constants. The propagation times vary up to 20 ns for different wires of the same chamber. In the following the calculation of the signal propagation time is described and compared to a measurement on a plane IV chamber.

9.1 Signal propagation speed

The length of the signal propagation path to the readout electronics can be calculated from the geometry of the chambers. To obtain the propagation time one has to know the propagation speed.

The speed of propagation of electromagnetic signals in a specific medium depends on the dielectric constant of the medium. The propagation speed can be calculated using the relation 9.1.

$$v = \frac{c}{\sqrt{\varepsilon_r}} \tag{9.1}$$

where

- v is the speed of propagation in the medium
- c is the speed of light in vacuum
- ε_r is the relative dielectric constant of the medium

For the polyethylene insulation used in a typical RG-58 coaxial cable, the value of the relative dielectric constant equals 2.3 [Mad05]. The speed of propagation of electric signals along such a type of cable is consequently 0.66 c. This corresponds to a inverse propagation speed of 5 ns/m.

Other experiments using similar gold plated tungsten wires as the ones used in the HADES drift chambers have measured inverse propagation speeds between 3.6 ns/m [Hir00] (determined from experimental data with cosmic rays) and 3.8 ns/m [VG01] (determined through the signal reflection on the wire).

A measurement of the signals propagation speed on a sense wire of a HADES drift chamber module has been performed. The observed speed is 0.86 c, which corresponds to an inverse speed of 3.89 ns/m. A description of the measurement is presented in section 9.2.

9.2 Propagation speed measurement

The measurement conducted to determine the speed of propagation of the pulser signals on the wires of the HADES drift chambers was realized on a long wire of a prototype 0° layer of a plane I chamber.

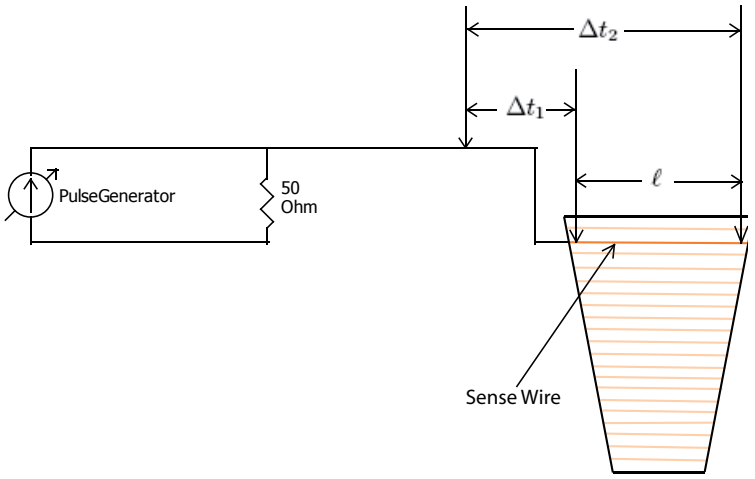

Figure 9.1: Schematic diagram of the measurement of the signals speed of propagation. A sharp signal is sent to one end of a signal wire. The propagation time on the wire equals the difference in the propagation time from a fixed point to each of the two wire ends. In the performed experiment the following values were measured: Δt_1=1.6 ns, Δt_2=4.4 ns, ℓ=72 cm.

The neighboring wires provide a similar environment as compared to a working chamber, neglecting, however, the effect of the different gas medium (air instead of $He - iC_4H_{10}$ mixture), and of the surrounding layers. A schematic diagram of the measurement is depicted in figure 9.1. From the measured values the propagation speed can be deduced to be $2.57 \times 10^8\ m/s$ or 0.86 c. Figure 9.2 shows the pulser signal at the reference point in yellow, and at both ends of the wire in light blue.

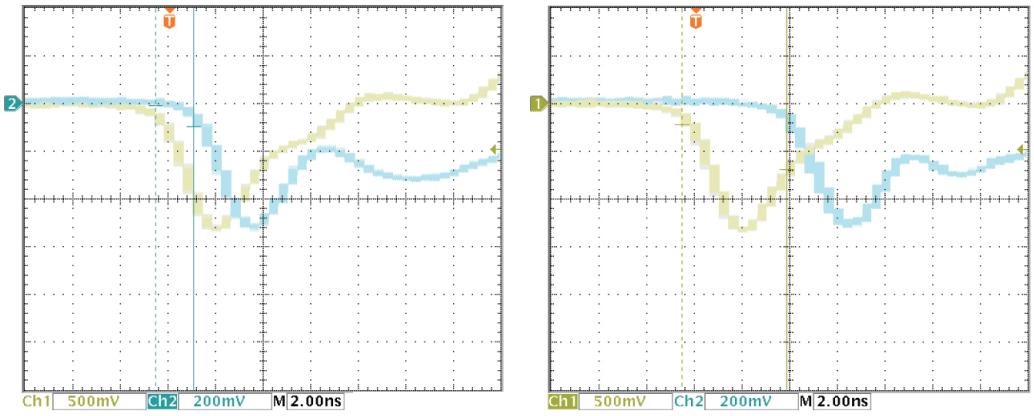

(a) (b)

Figure 9.2: The pulse as seen at the reference point (yellow), (a) at the near end, and (b) at the far end of the wire (light blue).

9.3 Propagation time verification

The propagation time of the pulser signals from the HV-box to the readout of each individual signal wire is defined by the geometry of the chamber. As a consistency check, the pulser signal has been sent along two different paths to the wires, along the field wires, and along the cathode wires. Figure 9.3 illustrates the signal path in both cases.

Since the field and cathode wires have different angles and different HV distribution lines, the propagation time in each case differs. Accordingly, the determined calibration constants vary. As shown in figure 9.4, the difference in the calibration constants can be reproduced making use of the information of the propagation path and speed of the signal in both cases. For the case of field wires, the propagation path is only well known, if the signal is sent exclusively to one

field layer. Sending the signal to more than one field layer simultaneously makes it difficult to define the propagation time of the recorded signal (see appendix B).

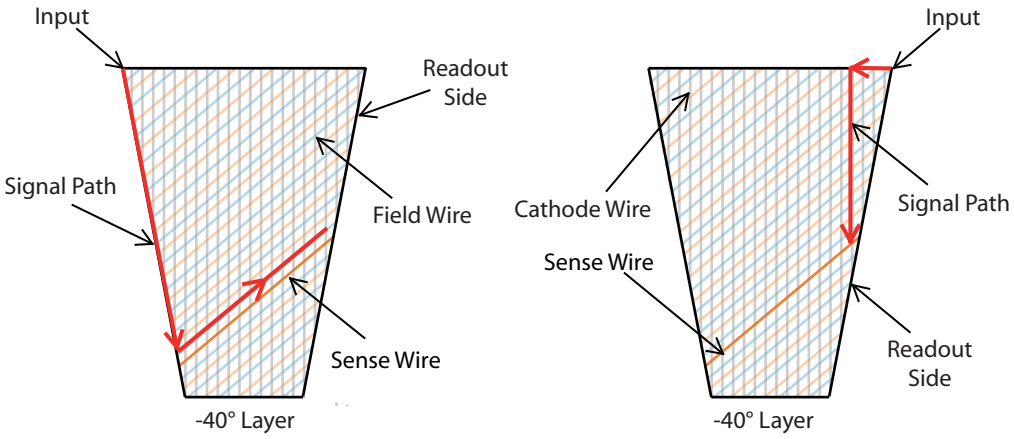

Figure 9.3: Pulser signals paths (red); (a) when coupling to the field wires, (b) when coupling to the cathode wires.

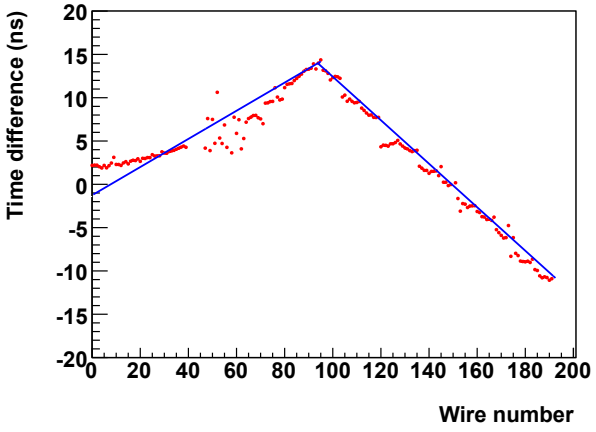

Figure 9.4: The signal propagation time difference between traveling along the field wires and traveling along the cathode wires: a) as calculated from the chamber geometry (blue line) and b) as deduced from the difference in the calibration constants in both cases (red points).

Chapter 10

Track reconstruction procedure

The reconstruction of particle trajectories through the drift chambers of the HADES spectrometer constitutes the final test of the validity and precision of the described calibration methods. In this chapter, the procedure and steps of the track reconstruction used in the HADES experiment are presented.
A single drift cell crossed by an ionizing particle does not deliver the position and direction information of the particle trajectory. Only after the spatial correlation of all drift cell crossed by the particle, the position and direction of the track can be obtained. The detection of the particle in 6 wire layers of a drift chamber provides redundant data to reconstruct the track in a single drift chamber or in a pair of two inner or outer chambers belonging to the same sector. The following steps summarize the procedure of the track reconstruction:

1. As a first step of the track reconstruction, the spatial correlation of fired drift cells is performed to search for the so called *wire clusters*. The wire clusters are defined using only the geometrical positions of the fired drift cell and neglecting the measured drift times. They represent a first approximation of the position and direction of the track segments. *Track candidates* are obtained through the matching of track segments in the inner and outer drift chambers of one sector which is performed on a virtual plane inside the magnetic field region.

2. After the reconstruction of the track candidates in the inner and outer drift chambers, the corresponding space positions of all fired drift cells are fitted by a model function taking into account the drift time information of the cells. The particle trajectory through a pair of inner or outer drift chambers is taken as a straight line assuming that the residual magnetic field in the drift chambers region is low enough and the particle momentum is large

enough to allow for neglecting the curvature of the track inside the chambers. The position and direction of the reconstructed track segments are significantly improved by the fit compared to the *wire clusters*. Candidates for which the fit fails or delivers bad results are removed in order to reduce the number of track fakes and to select on the quality of the reconstructed tracks (see section 10.2).

3. The inner track segments are matched with rings in the RICH detector while the outer track segments are matched with hit points in the META detectors (TOF|TOFino).

4. The momentum of the particle is determined by various algorithms making use of the bending of its trajectory inside the magnetic field region [SG03][Rus06].

5. Using the information of the particle momentum, time-of-flight and energy loss in the META detector and the drift chambers, the particle species can be identified. Furthermore, a reconstructed ring in the RICH detector and a detected electron shower in the PreSHOWER detector allow to efficiently identify leptons.

10.1 Cluster finding

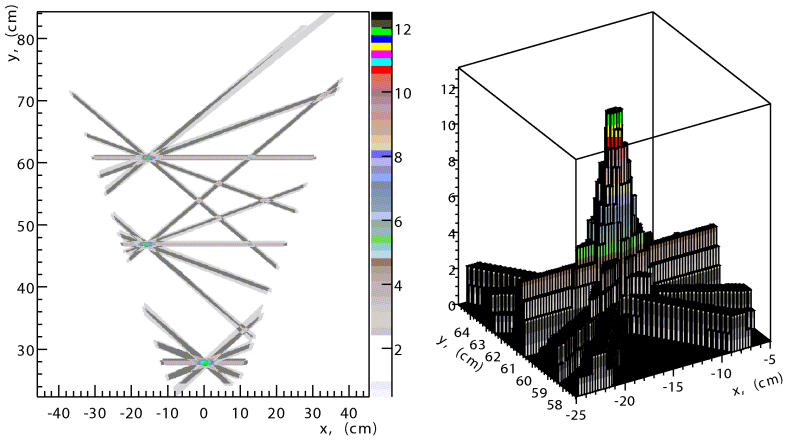

Figure 10.1: Projection of the drift cells in the cluster finding procedure [AP01].

The *cluster finding* [AP01] procedure is based on the assumption that straight line segments between pairs of inner and outer drift chambers are good approximations for the particle trajectory. The basic idea of the cluster finding is to project the volume of the fired drift cells onto a common plane. The position of the track is given by the maximum in the projected volumes *i.e.* the intersection of the fired drift cells (see figure 10.1).
The projection plane is located in the midplane of a chamber in the case of projecting the fired drift cells of one chamber alone. However, to guarantee the highest selectivity of real tracks and to lower the number of fakes, all fired drift cells belonging to a pair of inner or outer drift chambers are projected onto one plane. The projection plane is located in between the two chambers and is chosen such that the projections of the different drift cells are of similar size.
For the inner drift chambers the position and extension of the target along the beam axis are taken into account when searching for the wire clusters. The transverse dimension of the target is neglected. By taking into account the target position, the position of the maximum in the projected drift cells volumes provides the coordinates of the track segment in space and a list of drift cells belonging to the wire cluster.
The deflection of a charged particle by the toroidal magnetic field of the HADES magnet can be approximated by a single momentum kick on a nearly flat virtual plane [SG03] in the field region. Hence, when searching for wire clusters in the outer drift chambers, the same strategy is followed as for the inner ones except that the target position is replaced by the hit point of the inner segment on the virtual momentum-kick plane. This hit point represent the virtual track starting point after the deflection by the momentum kick in the magnetic field region. The cluster finding in the outer drift chambers is therefore based on the wire clusters found in the inner ones.
Matching the inner and outer segments together, one obtains a track candidate. Figure 10.2 depicts a schematic representation of the whole process.

The position resolution of the cluster finding algorithm is higher than the size of one drift cell. In general, the position resolution along the x-coordinate of the chamber is worse than the one along the y-coordinate. This difference is due to the orientations of the wires planes. The orientation of the wire planes have been chosen such that the best resolution is obtained in the direction of deflection of the particles by the magnetic field. For the inner drift chambers the resolution along the x-coordinate is $1.12 - 1.5\ mm$ and along the y-coordinate $0.8 - 1\ mm$. Due to the larger cell sizes of the outer drift chambers the obtained resolution along x is $3.9 - 4.8\ mm$ and along y is $2.9 - 3.3\ mm$.

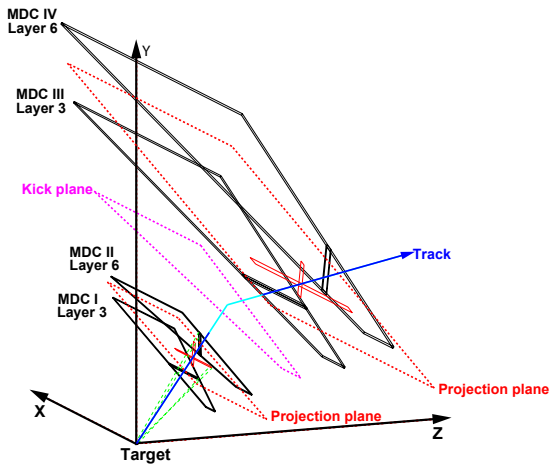

Figure 10.2: Schematic view of the track candidate search in the track reconstruction procedure [AP01]. The drift cells of a pair of two inner or outer drift chambers are projected onto a common plane. The projection of the drift cells for the inner chambers is done with respect to the target, whereas for the outer chambers the hit point of the inner segment onto the virtual momentum-kick plane is used.

10.2 Track fitting

The position resolution of the track candidates (see 10.1) does not meet the requirements of the HADES-experiment. In a second step, the precision of the reconstructed space points of the track candidates is improved by making use of the measured drift times in each drift cell and fitting the space coordinates of the track to a track model. Therefore, the drift times in each drift cell have to be converted into distances from the sense wires. The distance-time correlation of the drift cells (xt-*correlation*) is obtained from GARFIELD-simulations [Mar05] and verified through measurements.

The drift times measured by the TDC are the sum of the real drift time, the propagation time of the signal on the sense wire to the readout electronics, and the time-of-flight of the particle to the drift cell. The propagation time of the signal can be subtracted from the drift time since the position of the track is known: $t_{TDC} = t_{measured} - t_{wire}$. Since the remaining drift time t_{TDC} still contains a part of the time-of-flight of the particle, it is suitable to perform the track model fit in the time-coordinate and simultaneously extract the time-of-flight of the particle.

The ”straight line track” model used by the fit algorithm is defined inside one

drift chamber in the case of a fit to a single chamber (*single chamber fit*) or inside and between the two simultaneously fitted chambers (*combined chamber fit*). The latter method provides a better resolution and allows to efficiently remove fakes.

The following functional F for the least square minimization is evaluated for all drift cells of a track segment [Ier02]:

$$F = \sum_i \frac{(t^i_{drift} + t_{shift} - t^i_{TDC})^2}{(\Delta^i_{TDC})^2} \cdot w_i \tag{10.1}$$

t_{drift}	Drift time from GARFIELD-model
t_{shift}	Time shift of all cells
t_{TDC}	Drift time from TDC
w	Weighting constant (Tukey weight)
Δ_{TDC}	Error of drift time measurement

where i designates the individual drift cells and runs over all cells in the segment.

In the first iteration the time shift t_{shift} is calculated as the mean deviation of all drift time measurements from the known xt-correlation. This constant contains the time-of-flight of the particle to the drift chamber, as well as all deviations which are common to all drift cells considered in the fit. Such deviations can originate from errors in the determination of the calibration coefficients and constants, as well as changes in the operation conditions of the chambers which modify the xt-correlation of the drift cells.

The error of the drift time measurement Δ_{TDC}, as used by the functional, is known from the GARFIELD-simulations [Mar05].

The weighting factors w of the drift time measurements are calculated according to a *Tukey weight* distribution [Rus06]. The purpose of the weight is to minimize the influence of outliers on the result of the fit. Drift time measurements with a large deviation from the theoretical drift time are less weighted. Therefore, bad measurements or drift times belonging to electronic noise or other close-by tracks will be removed from the fit with a higher probability than the true measurements belonging to the track.

Chapter 11

Results

In this chapter, the results of the calibration of one plane IV chamber (third sector) using the external pulser method are shown, as well as a comparison between them and the results of the data based method. First the statistical properties of the distributions of the calibration constants will be analyzed, and second the effect of the two calibration methods on the quality of the track reconstruction will be discussed.

11.1 Distribution of the calibration constants

The calibration constants depend besides the cable lengths on the individual electronic components involved in the signal processing (see figure 11.1). TDC chips of one motherboard share the same cable from the common stop distribution system. Only the delays caused by the electronic components on the considered motherboard can cause a variation of the calibration constants of these chips. Individual delays for the different TDC channels which do not change over time will not influence the quality of the calibration. An upper limit of 2 ns for the components jitter can be deduced from figure 8.4.(c). In general, the calibration constants for all channels of one chamber do not vary strongly.

Figure 11.2 shows the distribution of the calibration constant of the calibrated plane IV chamber in the case of the data based method and the external pulser method. As seen from the figure, the variation of the values in the case of the external pulser method is less than in the data based method. The distribution of the calibration constants has a root mean square value (*RMS*) of 7.7 ns.

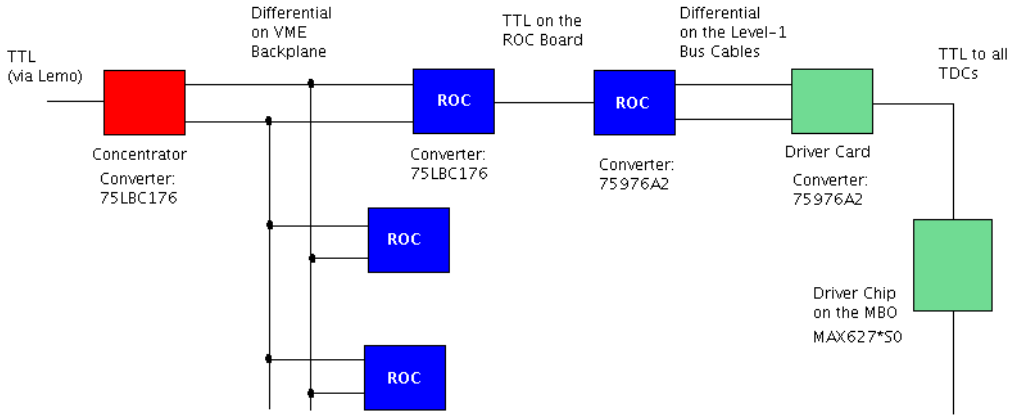

Figure 11.1: Schematic view of the CMS signal routing to the mini-VME crates and the motherboards. The red and blue components are described in figure 3.3, the green components are placed on the motherboards. Converters and driver chips which transform and transport the signal add different delay times to the propagation time of the signal.

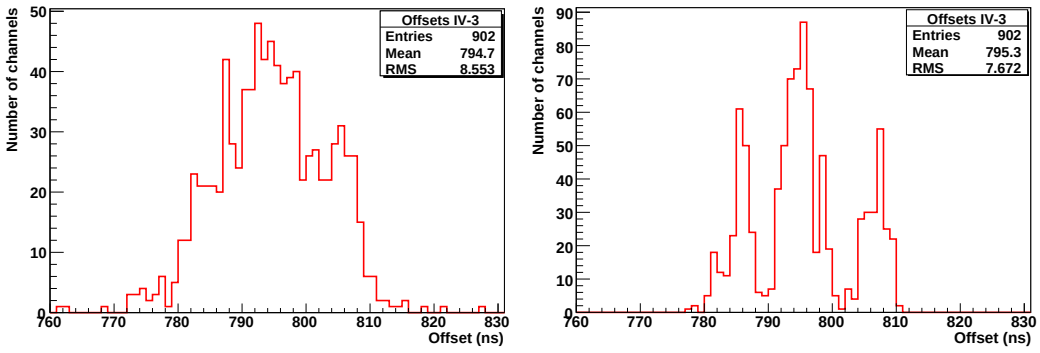

(a) (b)

Figure 11.2: The distribution of the calibration constants of a plane IV chamber around the mean value for (a) the data based method, (b) the external pulser method.

The calibration constant value depends on the position of the channel in the readout chain. In the data based method, the time-of-flight of the particle adds an additional dependence of the constants on the channel position. Figure 11.3 shows the dependence of the calibration constant on the cell number. The comparison between figures 11.3.(e) and 11.3.(f), shows that the scattering of the constants in the data based method is larger. The calibration constants vary throughout the same layer over a range of about 20 ns.

The variation of the time constants inside one motherboard is in the order of 1.5 ns for the case of the external pulser method. In the data based method, the constants scatter 5 times more with an average root mean square of 7.1 ns for one motherboard. All these values are summarized in table 11.1.

	External pulser method		**Data based method**	
Constants variation per	Mean value (ns)	RMS (ns)	Mean value (ns)	RMS (ns)
Chamber	7.8	NA	10.8	NA
Layer	5.9	0.6	9.1	2.9
Motherboard	1.5	0.5	7.1	5.3

Table 11.1: Comparison between the variation of the time constants in both calibration methods.

The mean value of the calibration constant in one motherboard depends on the position of the motherboard in the readout chain. Figure 11.5.(a) shows the mean value of the constants in each motherboard, and figure 11.5.(b) shows the position of the motherboard on the chamber frame and in the readout chain. The systematic in the mean values of the calibration constants of the motherboards can be attributed to the CMS distribution lines.

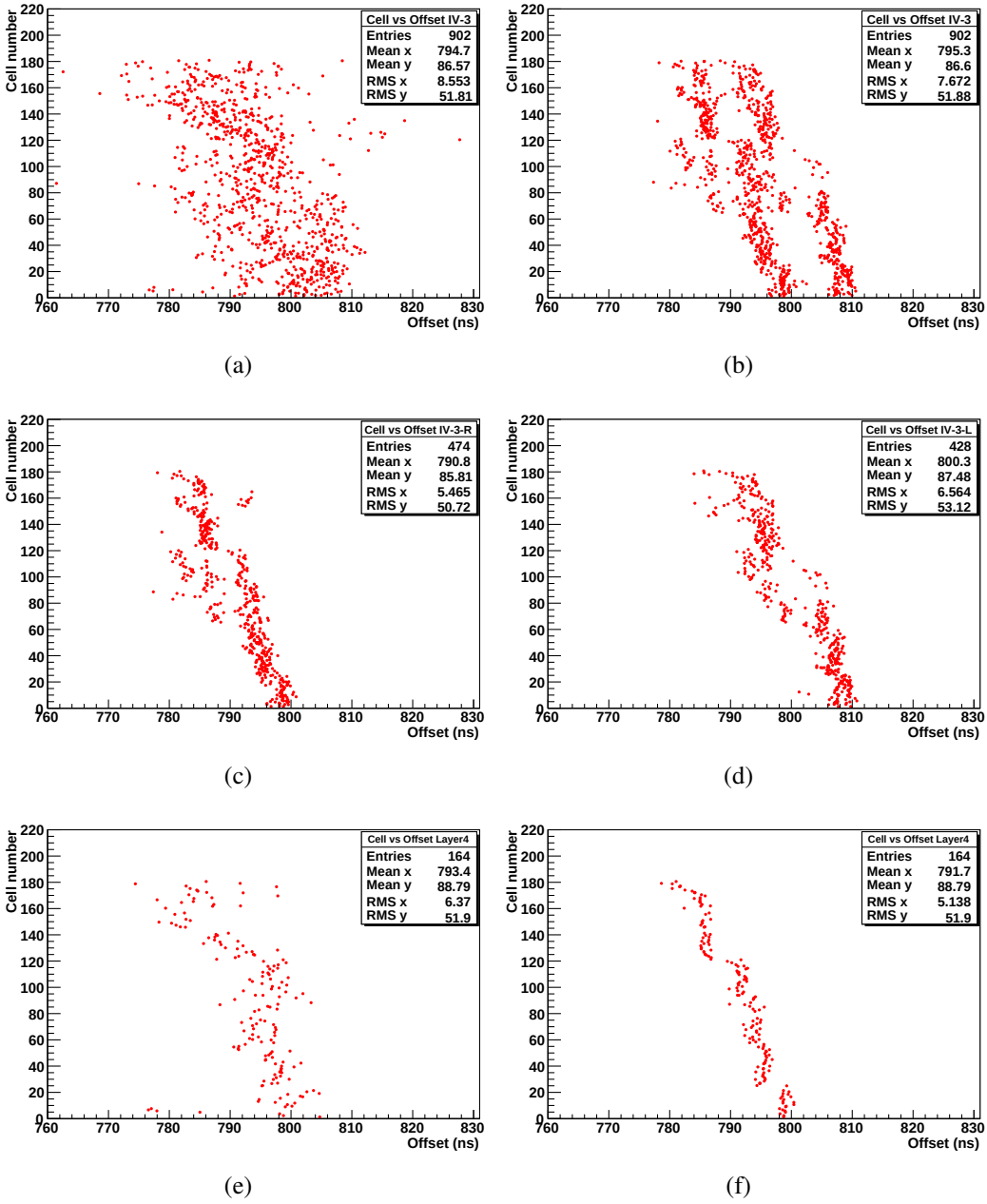

Figure 11.3: Variation of the calibration constants with the cell number for: (a) data based method, (b) external pulser method, (c) external pulser method for the three layers readout from the right side of the chamber, (d) external pulser method for the three layers readout from the left side of the chamber, (e) data based method for the fourth wire layer, and (f) external pulser method for the fourth layer.

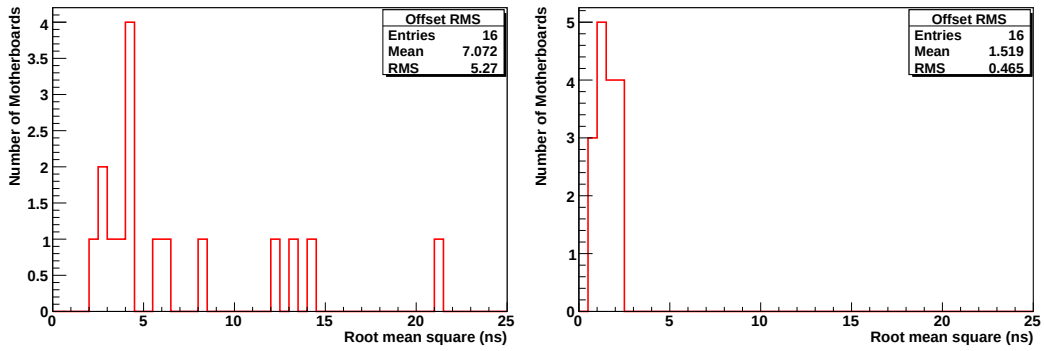

(a) (b)

Figure 11.4: The distribution of the root-mean-square value of the time constants distribution inside one motherboard in the case of: (a) the data based method (b) the external pulser method. The calibration constants vary throughout one motherboard about 1.5 ns around their mean in the case of the external pulser calibration.

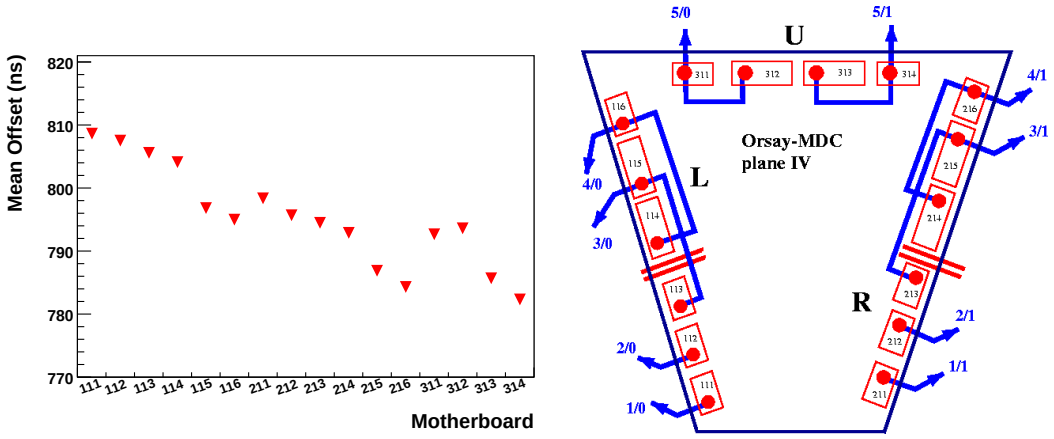

(a) (b)

Figure 11.5: (a) The mean value of the calibration constant as a function of the motherboard. (b) The positioning of the different motherboards on the chamber frame and in the readout chain. The changes in the mean values are correlated with the position of the motherboard in the readout system.

11.2 Results of the track reconstruction

As described in chapter 10, the calibration constants are essential parameters in the process of track fitting. In the following paragraphs, the results of the tracking process using the calibration constants of one plane IV chamber from both calibration methods will be presented. The used chamber is the one which was accessible out of the 24 chambers of the HADES MDC's. As mentioned in section 10.2, the time shift t_{shift} is the global constant subtracted from the measurements belonging to one particle trajectory to take into account the various contributions to the measured times other than the real drift time. Figure 11.6.(a) shows the distribution of the time shift as a function of the cell number for $p+p$ elastic scattering at a beam energy of 1.25 GeV when using the time constants deduced from the data based method. Systematic differences between the lower and upper parts of the chamber can be observed in the figure. Figure 11.6.(b) shows the projection of the time shift distribution for selected channels from the two regions. The mean value of the distribution differs between the two projections by about 2.9 ns. Looking at

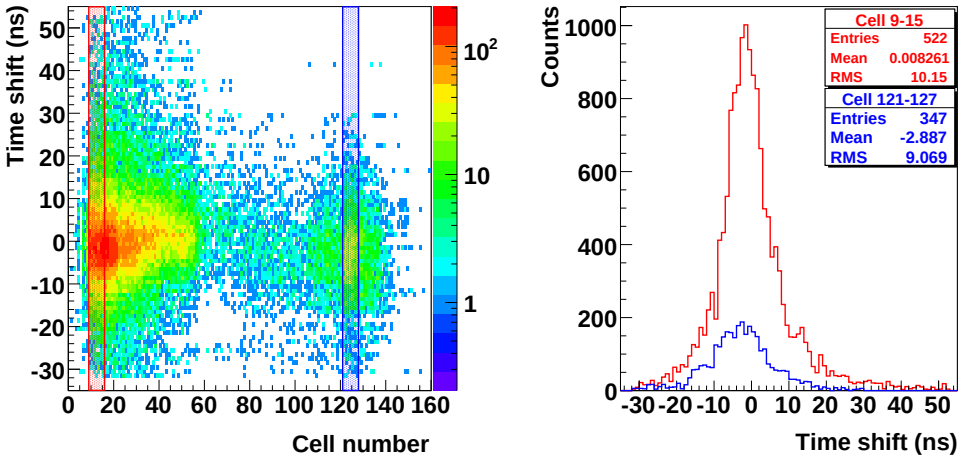

(a) (b)

Figure 11.6: Data based method: (a) The time shift distribution of a plane IV chamber for selected $p+p$ elastic events, (b) Projections of the distribution for cells 9-15 (red) and for cells 121-128 (blue).

the same plot when using the calibration constants deduced by the external pulser method, the difference in the mean value of the distribution in the two regions grows up to about 7.9 ns (see figure 11.7). This difference is due to the system-

atic effects introduced by the time-of-flight of the particles which is included in the data based method and is discussed in detail in the next paragraphs.

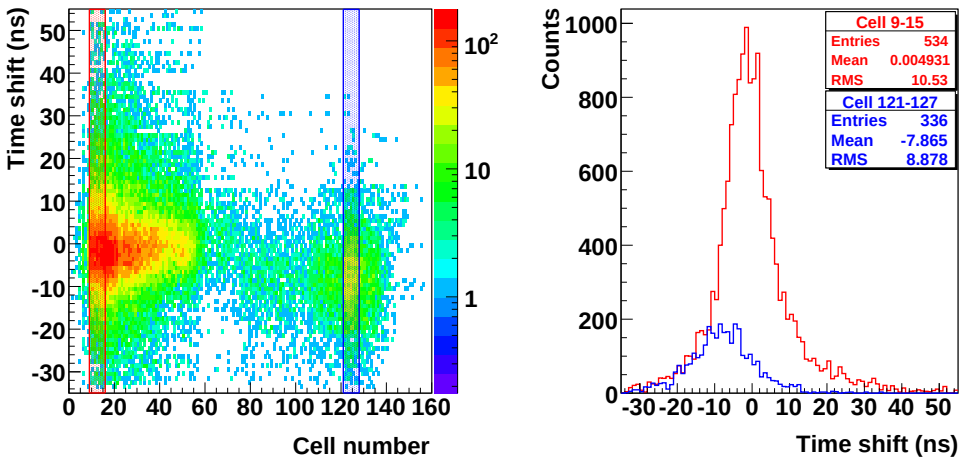

(a) (b)

Figure 11.7: External pulser method: (a) The time shift distribution of a plane IV chamber for selected $p + p$ elastic events, (b) Projections of the distribution for cells 9-15 (red) and for cells 121-128 (blue).

As already mentioned in chapter 7, the momenta of the particles crossing the drift chamber depend on the polar angle, which in turn is correlated with the cell number in the chamber. For elastic scattered protons this correlation is even more strict than for heavy ion reactions. Figure 11.8 shows the dependence of the particle momentum on the cell number of the first 0° layer of a plane IV chamber as obtained from simulated $p + p$ elastic events at a beam energy of 1.25 GeV. Therefore the time-of-flight of the detected protons depends also on the drift cell number. Figure 11.9.(a) shows the simulated time-of-flight distribution of the detected protons as a function of the cell number of the first 0° layer of a plane IV chamber. Figure 11.9.(b) shows the value of the minimum time-of-flight of these protons to the corresponding drift cell. The difference between the minimum time-of-flight for cell number 10 and 125 is 4.5 ns.

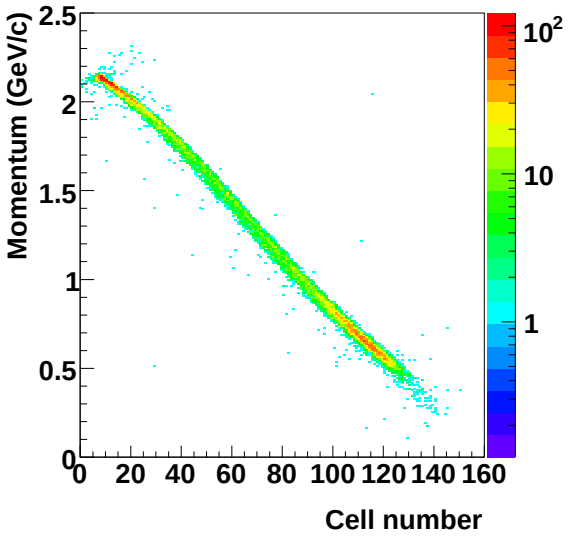

Figure 11.8: The momentum distribution of the detected protons in simulated $p + p$ elastic scattering events at a beam energy of 1.25 GeV against the drift cell number of the first 0° layer of a plane IV chamber.

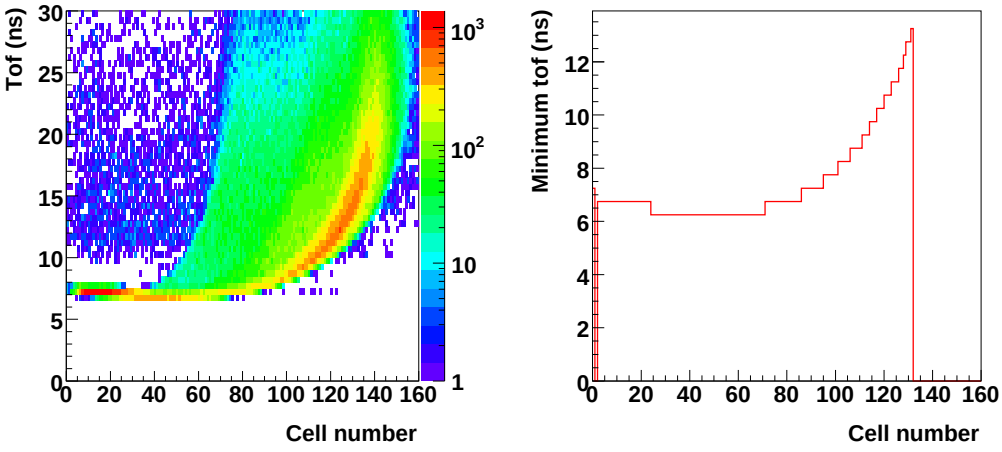

(a) (b)

Figure 11.9: (a) Time-of-flight distribution versus cell number of the sixth layer of a plane IV chamber for detected protons from simulated $p + p$ scattering at a beam energy of 1.25 GeV. (b) The minimum time-of-flight of the protons to the wire plane versus the cell number.

Adding the minimum time-of-flight of the protons to the calibration constants deduced by the external pulser method, the following picture of the time shift distribution is obtained (see figure 11.10). The difference in the mean value of the time shift distribution between the upper and lower regions of the chamber is now reduced to about 3.3 ns which is similar to the value obtained from the data based method.

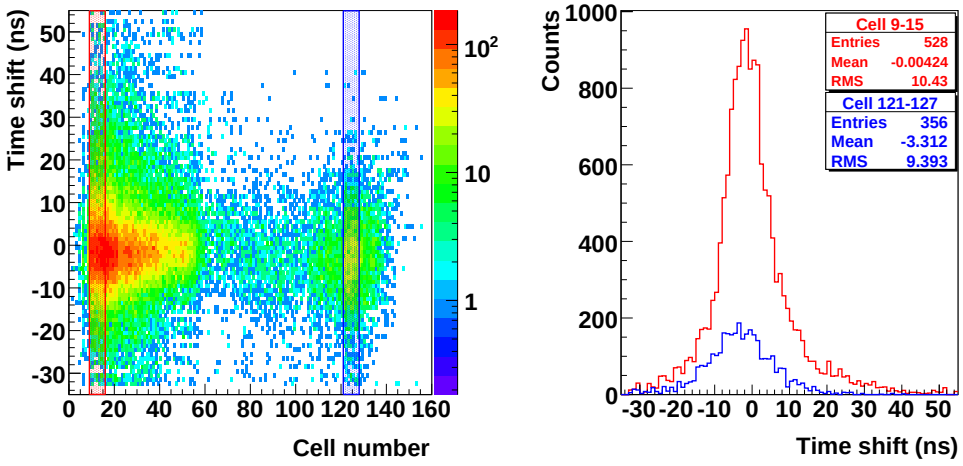

(a) (b)

Figure 11.10: External pulser method including particles minimum time-of-flight information: (a) The time shift distribution of a plane IV chamber for selected $p + p$ elastic events, (b) Projections of the distribution for cells 9-15 (red) and for cells 121-128 (blue).

In order to understand why adding the minimum time-of-flight of the protons doesn't bring the mean of the time shift distribution to the same value, one has to recall that the mean time-of-flight of the protons to reach the drift cell can be significantly different from the minimum time of flight –especially with increasing the cell number– as seen in figure 11.9.(a). Accordingly, shifting the time constants by the minimum time-of-flight of the protons, doesn't move the mean of the time shift of all cells to the same point. This results in the remaining 3.3 ns difference which are still observed. Unfortunately, obtaining an exact value for the mean time-of-flight of the protons to each drift cell was not possible in the scope of this work as it requires a sophisticated simulation of the spectrometer geometry and trigger conditions.

The calibration constants deduced from the data based method already con-

tain information about the minimum time-of-flight of the particles emitted in the reactions which cross the drift cell. For that reason they show almost the same difference in the time shift distribution between the lower and upper part of the chamber as the external pulser calibration constants corrected with the minimum time-of-flight information. The small change in the observed difference arises because the sample of particles, for which the time of flight information is taken, is different in both cases (for the data based method: all types of particles emitted in the reaction of the two protons; for the external pulser method: only the protons undergoing elastic scattering).

The time shift distribution is used to obtain the global correction constant of the time constants deduced from the external pulser method (see 8.2). The value of the global correction constant is chosen such that, the mean value of the time shift distribution at the lower part of the chamber lies at zero. The time shift distribution is produced using the new calibration constants, and after some iteration the value of the global correction constant is obtained.

11.2.1 Quality comparison

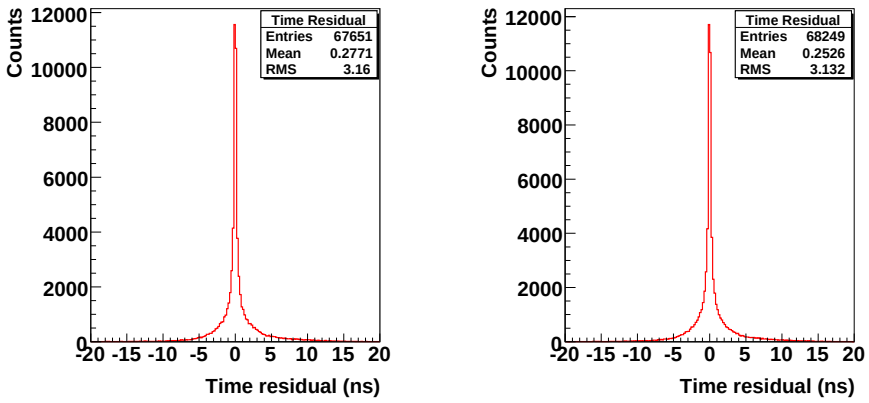

(a) (b)

Figure 11.11: Distribution of the time residual using: (a) data based calibration method, (b) external pulser method. The number of measurements accepted by the fit algorithm is increased by about 1% using the external pulser time constants. Also the RMS of the distribution is smaller in the case of the external pulser.

The quality of the calibration parameters can be checked by means of the residuals of the measured and calculated drift times as provided by the track fitting

algorithm (see 10.2). The error in the calibration constant of one cell crossed by a particle trajectory relative to other cells crossed by the same particle can not be corrected using the time shift discussed above, if it is not common to all cells. Therefore, they lead to a wider residual distribution since the registered drift time deviates from the real time. Figure 11.11 shows the residual distribution using the time constants from both calibration methods. The number of measurements accepted by the fit algorithm is increased by about 1% using the external pulser time constants. The RMS value of the distribution is also about 1% less in the case of the external pulser constants. Table 11.2 offers a comparison between the quality check results of both calibration methods.

	External pulser method		**Data based method**	
Cell number	Accepted measurements	Residuals RMS (ns)	Accepted measurements	Residuals RMS (ns)
0-60	58815	2.79	58371	2.79
60-100	2029	6.6	2045	6.76
100-160	7405	4.22	7235	4.33
All cells	68249	3.13	67651	3.16

Table 11.2: Comparison of the quality of the two calibration methods. The external pulser method provides slightly better results in the track reconstruction procedure.

11.3 Conclusion

Although the calibration constants obtained by the external pulser method have a better accuracy and do not contain the systematic errors contained in the data based method, the results of the track reconstruction process is not improved significantly. The residuals obtained from the fit are dominated by uncertainties of the drift time measurement (1-3 ns), the fluctuation in the experiment trigger ($\sim$ 5 ns), the intrinsic misalignment of the chamber wires and the ability of the track fitting algorithm to converge to the proper minimum and not by the corrections determined in this thesis.

Chapter 12

Summary and Outlook

The following points summarize the results of this work:

- Coupling an external pulse to the potential wires of the HADES drift chambers through their individual high voltages boxes induces time correlated pulses on the signal wires of the chamber.
- The propagation speed of the signal on the wires of the chambers has been successfully measured.
- The propagation time of the signal on the chamber frame and the different wires of the chamber to the readout electronics has been calculated and confirmed by a measurement.
- The accuracy of the method exceeds the resolution of the drift time measurement itself.

moreover:

- The calibration constants of all TDC channels belonging to the same motherboard do not vary considerably. The variation of the constants throughout one motherboard is in the order of 2 ns which is in the accuracy range of the method and of the drift time measurement.
- The values of the calibration constants depend on the position of the motherboard and measuring channel i.e. on the distance the "common stop signal" has to travel to reach the considered channel.

- The scattering of the calibration constants deduced from the external pulser method is much less than in the case of the data based method. Statistical aspects, trigger fluctuations and noise heavily affect the precision of the data based method.
- The new method provides calibration constant parameters independent of the time-of-flight of the particles. As long as the electronic setup stays unchanged, the parameters determined for a specific experiment can be used also for subsequent experiments.
- The quality of the calibration parameters obtained from the external pulser method has been used to reconstruct tracks. The resulting precision is the same as obtained with those of the data based method.

Outlook

The investigation of the new method for the calibration of the HADES MDC's has been successfully performed on one module of the drift chambers which was easily accessible. The results of the investigations are very promising, the method has been found to be accurate, fast and robust.
The new method is independent of the experiment data, it can be performed before or after an experiment, or even during the experiment. In contrast to the old method, the new method decouples the calibration of the drift chamber from the alignment. Hence, the alignment of the drift chamber, especially the internal geometry, can be more efficiently performed in the future.
To use the new method for the calibration of the MDC's in the future experiments, the high voltage boxes of all chambers have to be modified in order to allow for a signal coupling to the cathode wires of the chambers. The design of the chamber makes it impossible for a simultaneous calibration of all layers when coupling the pulser signal to the field wire of the chamber. The calculation of the propagation time in that case becomes very complicated and can change by changing the coupling conditions or the input signal (see appendix B). Modifying the high voltage boxes, although requiring a considerable effort, should be carried out. The new method, being easy and robust, will save computing time and the effort to adapt the parameters of the other method to the varying experimental conditions.

Appendix A

TDC spike suppression mode

An important feature of the TDC's used in the readout electronic system of the HADES drift chambers is the so-called spike suppression mode. This feature is used to reduce the amount of noise detected by the TDC. For each leading edge detected by the TDC, the algorithm looks for a trailing edge in a specific time range of up to 23 ns after the leading edge. If a trailing edge is detected in the specified range, the measurement is considered as noise since the difference between the two edges is not in the range of that for real particle signals. Both measurements are therefore discarded and the TDC stays ready to measure the next coming leading edge.
Refereing to figure 8.3, due to the reflections and oscillations superimposed on the external pulser signal induced on the signal wire, the pulse on the wire doesn't develop smoothly with time. Instead, it can be represented as a sequence of partially overlapping individual pulses which exhibit flat step-like regions. The ASD8 chip differentiates the input signal before discriminating it. Differentiating a step gives essentially zero. After the step, the signal edge continues to develop with time, and the ASD8 chip creates a new signal. The output of such a step signal on the signal wire is many digital pulses of short widths for each step in the signal. The output pulses have a smaller width as compared to the original signal and are very close to each other since the width of the steps is not long.
These many short close pulses may conflict with the spike suppression function of the TDC. They are considered as noise and are discarded. Moreover, since the pulses are very close to each other, the TDC algorithm fails sometimes to keep track of the sequence of leading and trailing edges. It may disregard a short pulse and assign a wrong TDC channel number to the subsequent pulse. The result is that the timing of the detected pulses is sometimes totally wrong depending on the detailed shape of the input pulse.

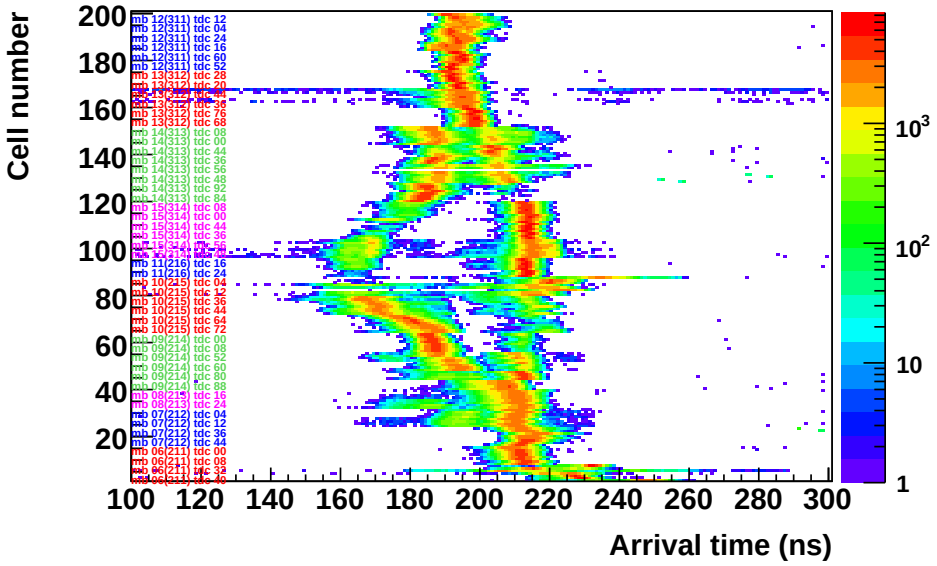

(a)

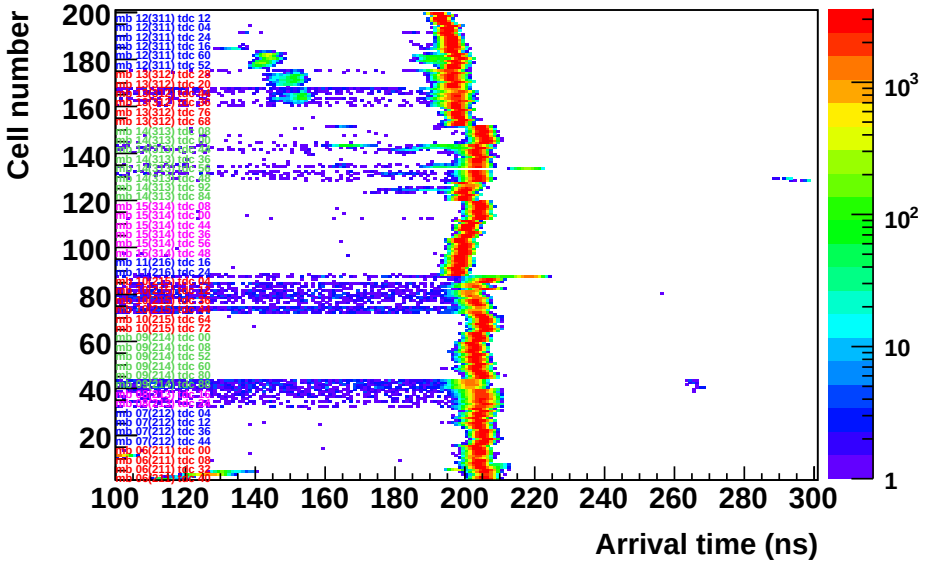

(b)

Figure A.1: The pulser spectrum of the sixth layer of a plane IV chamber as a function of the signal wire number: (a) when switching on the spike suppression mode, (b) when switching off the spike suppression mode. The text to the left shows the hardware address of the wire; different colors indicate different motherboards. For some channels a second peak arises in the spectrum at a position of up to 80 ns before the real peak. Switching off the spike suppression mode essentially eliminates this phenomenon. The second peak phenomenon extends over different motherboards with the same trend.

For the purpose of the MDC calibration using the external pulser, and since it is impossible to avoid the reflections superposed on the external pulser signal, the TDC spike suppression mode has been switched off during the data taking of the external pulser calibration. Figure A.1 shows the effect of the spike suppression mode on the registered pulser spectrum for the sixth layer of a plane IV chamber.

Appendix B

Proper signal path

The discussion presented in section 9.3 has proven that the propagation time of the external pulser calibration signal is well determined in the both cases of sending the pulse along the field wires and along the cathode wires of the chamber. Nevertheless, this statement is only true when the pulse is sent to the neighboring potential wires of only one sense layer for which the calibration parameters are to be determined. If all channels of a chamber are to be calibrated, sending the calibration pulse along the cathode wires of the chamber instead of the field wires is mandatory. The reason for that is described in the following paragraphs.
All wires of a drift chamber are coupled by the capacitance between each pair of them. A pulse on the field wires of one layer of a chamber induces signals on the sense wires of all layers of that chamber. The induced signals can vary in the rising|falling time of their leading|trailing edges, and can have a delay with respect to the time of the original pulse.

The design of the chamber is made such that each neighboring two layers are readout from opposed sides of the chamber. The high voltage of each field layer is supplied from the side of the chamber opposite to the readout side of the particular layer. The calibration pulse has therefore to propagate along the whole length of the field|sense wire to reach the readout electronics of the sense wires of the corresponding layer. However, the calibration pulses of the two neighboring layers are sent to the wires along the same side of the chamber as the readout electronics of the layer considered. If all calibration pulses are sent to the field wires simultaneously, the signal induced on a sense wire by the pulse on the field wire of the neighboring layer can reach the readout electronics before the signal induced from the field wires of the same layer. However, the rise time of the signal in both cases will be different. Figure B.1.(a) illustrates this problem. The pulse on each shown field wire will induce a signal on the considered sense wire. The order of the signals as they will reach the readout electronics of the wire is indicated by the

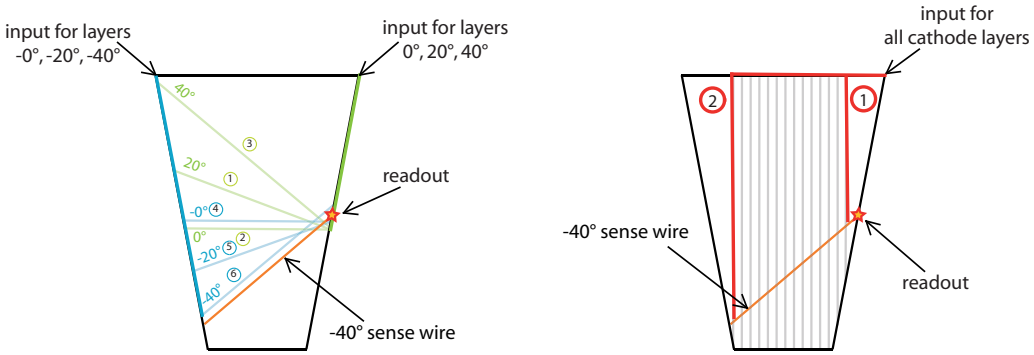

(a) (b)

Figure B.1: (a) The external pulser signal is sent to all field wires of the chamber simultaneously via the two input points at the left and right of the chamber. The signal on the considered $-40°$ wire can be induced by the pulse on any of the shown field wires. The numbers show the field wires ordered by the geometrical distance between their point of coupling to the high voltage distribution line and the readout end of the considered sense wire. The earliest signals come from the field wires whose pulser input is at the same side of the chamber as the readout electronics of the considered sense wire. (b) In the case of sending the calibration pulse to the cathode wires, the situation for pulsing a single layer or all layers simultaneously is similar, since all layers have their pulser input at the same position on the chamber frame. Path 1 represents the first, and path 2 the last signal which will reach the readout in all cases.

numbers on the corresponding field wire. The signals have been ordered taking only geometrical distances into account and neglecting the rise time of the signals. Taking the cathode layer between each two sense|field layers into account, the situation becomes more complicated. The calculation of the propagation time of the signal in such a case becomes difficult.

Assuming that the signal of one layer is coupled with the same rise time to the wires of the other layers directly at the beginning of the sense wires seems to be non applicable. This assumption would imply that the first signal seen by the sense wires of a $0°$ layer are induced from pulses on the field wires of the neighboring $-0°$ layer. The time difference between these fastest signals and the signals induced on the wires by the pulses on the field wires of the same layer would be in such case the time needed to cross the wire *i.e.* the propagation time along the wire. Figure B.2 shows the difference in the recorded signal time in a $0°$ layer once sending the calibration pulse exclusively to the considered layer and

once sending it simultaneously to all field layers, as a function of the wire number. The blue line represents the propagation time of a signal along the wire.

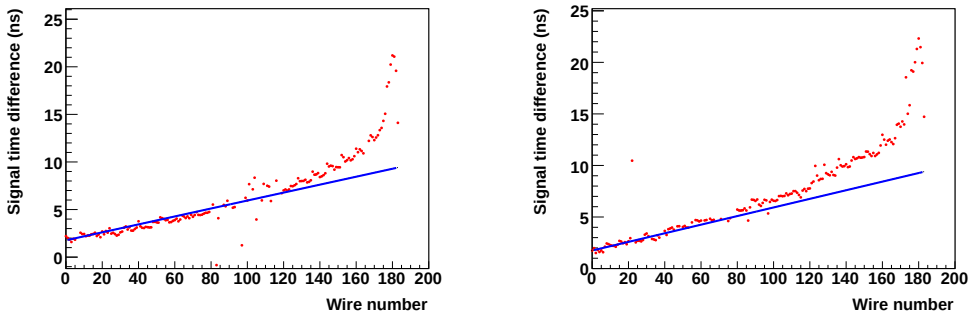

(a) (b)

Figure B.2: The difference in the recorded signal time for the case of sending the calibration pulse to the considered field layer only and sending it to all field layers at the same time (red) as a function of the wire number. (a) Shown for the first 0° layer, (b) for the second 0° layer. The blue line represents the wire length in both cases.

A clear deviation of the time difference from the calculated line is observable, thus confirming that the simple assumption mentioned before is not valid, and that the calculation of the propagation time in the case of pulsing all field layers simultaneously is not possible. On the other hand, the cathode layers have almost identical signal paths. Therefore, sending the pulse to all cathode layers at once would allow to calibrate all channels simultaneously without having a problem to calculate the signal propagation time.

Bibliography

[5sp05] Spice simulation by Win Spice. http://www.winspice.com/, 2005. 44

[AP01] G. Agakishiev and W. Pechenov. The dubna track reconstruction manual. interner HADES report, Dezember 2001. 54, 55, 56

[Böh99] M. Böhmer. Das Auslesesystem für den Ringabbildenden Cherenkovdetektor im HADES Spektrometer. Diplomarbeit, Physik-Department der Technischen Universität München, Institut E12, 1999. 5

[Bou94] R. Bouclier et al. *Nucl. Instrum. Meth.*, A 350:464, 1994. 10

[Bou96] R. Bouclier et al. *CERN CMS technical note 96-038*, 1996. 11

[Gar98] C. Garabatos et al. Optimisation of low-mass drift chambers for HADES. *Nucl. Instrum. Meth.*, A 412:38–46, 1998. 11

[Hir00] H. Hirano et al. A high-resolution cylindrical drift chamber for the KEK B-factory. *Nucl. Instr. Methods*, A(455):294–304, 2000. 50

[ICR84] ICRU Report No.37. Stopping Powers for Electrons and Positrons, 1984. 16

[Ier02] A. Ierusalimov. New version of dubna track fitter. interner HADES report, Juni 2002. 57

[Lip00] C. Lippmann. Aufbau und Inbetriebnahme eines Gasqualitätsmonitors für die HADES-Driftkammern. Diplomarbeit, Physik-Fachbereich der Johann-Wolfgang- Goethe-Universität Frankfurt a.M., 2000. 6

[Mad05] tyco electronics. Data sheet of several electronic cables. USA: 1-877-MADISON (623-4766). 02.2005, 2005. 50

[Mar05] J. Markert. *Untersuchung zum Ansprechverhalten der Vieldraht-Driftkammern niedriger Massenbelegung des HADES Experiments*. Disseration, Johann Wolfgang Goethe-Universität Frankfurt am Main, 2005. 21, 22, 34, 41, 42, 56, 57

[Mdc04] Official HADES MDC webpage; http://www-hades.gsi.de/mdc/, 2004. 13

[New93] F. M. Newcomer. A Fast Low Power, Amplifier-Shaper-Discriminator for High Rate Straw Tracking Systems. *IEEE Transactions on Nuclear Science*, 40(4):630, August 1993. 12, 29

[PDG06] Particle data group. 27. passage of particles through matter; http://pdg.lbl.gov/, 2006. 15, 17

[Rus06] A. Rustamov. *Exclusive η Meson Reconstruction in Proton-Proton Collisions at 2.2 GeV with the HADES Spectrometer and High Resolution Tracking*. Dissertation, Fachbereich Physik, Technische Universität Darmstadt, Darmstadt, 2006. 54, 57

[Sau77] F. Sauli. *Principles of operation of multiwire proportional and drift chambers*. Lectures given in the academic training programme of CERN, CERN; European Organization For Nuclear Research, Geneva, 1977. 17, 18, 19, 20, 21, 44

[SG03] M. Sánchez-García. *Momentum reconstruction and pion production analysis in the HADES spectrometer at GSI*. Dissertation, Universidade de Santiago de Compostela, 2003. 54, 55

[Str98] J. Stroth. A Low-mass Tracking System for HADES. *WCC 98, Vienna*, 1998. 10

[TDC98] ASIC Design Center Dokumentation, Funktionsbeschreibung für den HADES Drift Chamber TDC incl. Änderungen für HADES Rev. 02 (Redesign), 1998. 12

[VG01] T. Sluijk V. Gromov. Electrical properties of various types of straw tubes considered for the LHCb Outer Tracker. Internal report, NIKHEF, Amsterdam, Januar 2001. 50

[Wüs98] J. Wüstenfeld et al. A TDC ASIC for the HADES Drift chamber readout. *Deutsche Physikalische Gesellschaft, Frühjahrstagung*, HK 56.69, Poster, Bochum, März 1998. 32, 33

[Zum98] Peter W. Zumbruch. Entwicklung und Aufbau eines Teststandes zur automatisierten Qualitätskontrolle der HADES-Driftkammer-Analogausleseelektronik. Master's thesis, Technische Universität Darmstadt, 1998. 33

[Zum01] P. Zumbruch et al. Calibration Strategy and Performance of the HADES Drift Chamber Tracking System. *Deutsche Physikalische Gesellschaft, Frühjahrstagung*, HK 9.2, Poster, Erlangen, März 2001. 34

[Zum05] P. W. Zumbruch. Dissertation, Fachbereich Physik, Technische Universität Darmstadt, Darmstadt, 2005. 36